

## PROCEEDINGS A

[rspa.royalsocietypublishing.org](http://rspa.royalsocietypublishing.org)

Research



Article submitted to journal

### Subject Areas:

mechanical engineering, differential equations

### Keywords:

nonlinear dynamics, double Hopf bifurcation, center manifold reduction, machine tool vibration

### Author for correspondence:

Tamas G. Molnar

e-mail: [molnar@mm.bme.hu](mailto:molnar@mm.bme.hu)

# On the analysis of the double Hopf bifurcation in machining processes via center manifold reduction

T. G. Molnar<sup>1</sup>, Z. Dombovari<sup>1</sup>, T. Inspurger<sup>2</sup> and G. Stepan<sup>1</sup>

<sup>1</sup>Department of Applied Mechanics, Budapest University of Technology and Economics, H-1111 Budapest, Hungary

<sup>2</sup>Department of Applied Mechanics, Budapest University of Technology and Economics and MTA-BME Lendület Human Balancing Research Group, H-1111 Budapest, Hungary

The single-degree-of-freedom model of orthogonal cutting is investigated to study machine tool vibrations in the vicinity of a double Hopf bifurcation point. Center manifold reduction and normal form calculations are performed to investigate the long-term dynamics of the cutting process. The normal form of the four-dimensional center subsystem is derived analytically, and the possible topologies in the infinite-dimensional phase space of the system are revealed. It is shown that bistable parameter regions exist where unstable periodic and, in certain cases, unstable quasi-periodic motions coexist with the equilibrium. Taking into account the non-smoothness caused by loss of contact between the tool and the workpiece, the boundary of the bistable region is also derived analytically. The results are verified by numerical continuation. The possibility of (transient) chaotic motions in the global non-smooth dynamics is shown.

## 1. Introduction

Improving the productivity of metal cutting operations is highly important for the manufacturing society. The occurrence of harmful vibrations during machining – known as machine tool chatter – limits the achievable productivity. Therefore, studying the dynamics of machine tool chatter is an active field of research.

© The Authors. Published by the Royal Society under the terms of the Creative Commons Attribution License <http://creativecommons.org/licenses/by/4.0/>, which permits unrestricted use, provided the original author and source are credited.

1 The aim of analysing machine tool vibrations is to identify those regions in the space of the  
 2 technological parameters, which are associated with chatter-free manufacturing processes. These  
 3 parameter regions are typically illustrated in the plane of the spindle speed and the depth of cut;  
 4 this picture is called stability lobe diagram or stability chart. The first successful efforts to describe  
 5 chatter and to derive stability charts are presented in the works of Tobias [1] and Tlustý [2].

6 Machine tool vibrations are described by delay-differential equations (DDEs), since the chip  
 7 thickness, which determines the cutting force, is affected both by actual and delayed tool  
 8 positions due to the surface regeneration effect. Since DDEs have infinite-dimensional phase  
 9 space representation [3], the dynamics of machine tool chatter is rich and intricate. Furthermore,  
 10 the modelling DDEs are typically nonlinear, since the cutting force is a nonlinear function of the  
 11 chip thickness [4].

12 Here, we restrict ourselves to the analysis of autonomous DDEs, which are the typical  
 13 models of turning operations. Along the stability boundaries (or stability lobes) of turning, Hopf  
 14 bifurcation occurs, which gives rise to a periodic solution of the nonlinear system. This periodic  
 15 solution plays an important role in determining the global dynamics of the cutting process that  
 16 may involve the high frequency self-excited vibration called chatter. The effect of nonlinearities  
 17 on the occurrence of machine tool chatter was investigated for example in [5–8], whereas the  
 18 bifurcation analysis of machining processes can be found in [9–14] for turning and in [15] for  
 19 milling operations. The theory of Hopf bifurcation in DDEs is covered by [3,16–19]. The most  
 20 popular approaches for bifurcation analysis are the rigorous center manifold reduction [20] and  
 21 the method of multiple scales [12,13]. Note that other methods also exist for the computation of  
 22 periodic solutions [21], e.g. the method of small parameters or the theory of averaging [5,22–26].

23 In this paper, we analyse the intersection of stability boundaries where double Hopf  
 24 bifurcation takes place. The double Hopf bifurcation complicates the dynamics of metal cutting by  
 25 giving rise to a quasi-periodic solution [27]. Examples for the analysis of double Hopf bifurcation  
 26 can be found in [28–38] for various dynamical systems. The double Hopf bifurcation in metal  
 27 cutting was analysed in [39] using the method of multiple scales. Now we extend this work by  
 28 analysing a slightly different model using center manifold reduction. In particular, we investigate  
 29 the possible topologies in the phase portraits of the system near the double Hopf bifurcation and  
 30 we also discuss the phenomenon of bistability. We verify the results by numerical continuation.  
 31 Continuation of periodic solutions of nonlinear DDEs can be carried out by the software DDE-  
 32 BIFTOOL [40], whereas the arising quasi-periodic solution can be computed by the software  
 33 KNUT [41,42] or by the algorithm used in [15]. In this paper, we use the latter algorithm to verify  
 34 the results of center manifold reduction.

35 The rest of the paper is organised as follows. Section 2 presents the mechanical model of  
 36 turning. Section 3 discusses the linear stability analysis, whereas Sec. 4 shows the bifurcation  
 37 analysis using center manifold reduction. The resulting stability charts and bifurcation diagrams  
 38 are presented together with implications on the global dynamic behaviour in Sec. 5. Conclusions  
 39 are drawn in Sec. 6.

## 40 2. Equation of Motion

41 We consider the single-degree-of-freedom model of orthogonal cutting shown in Fig. 1(a). The  
 42 equation of motion for the tool can be given in dimensionless form as follows (see [11] for details):

$$43 \quad x''(t) + 2\zeta x'(t) + x(t) = w \left( (x(t - \tau) - x(t)) + \eta_2 (x(t - \tau) - x(t))^2 + \eta_3 (x(t - \tau) - x(t))^3 \right), \quad (2.1)$$

44 where  $t$  is the dimensionless time measured by the time period of the free undamped natural  
 45 oscillation of the system,  $x$  indicates the dimensionless position of the tool with respect to the  
 46 constant theoretical chip thickness set to have unit length in Fig. 1, and  $\zeta$  is the damping ratio  
 47 of the dominant vibration mode of the system. The right-hand side of Eq. (2.1) is proportional  
 48 to the variation of the dimensionless,  $x$ -directional cutting force component, which is assumed  
 to be a cubic polynomial function of the dimensionless chip thickness variation  $x(t - \tau) - x(t)$ .

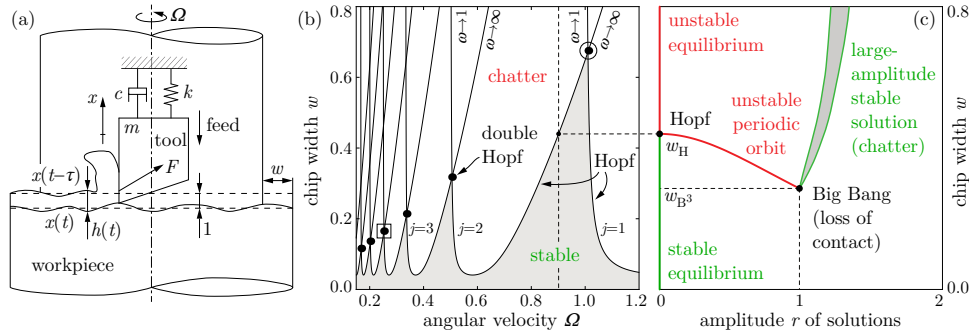


**Figure 1.** Single-degree-of-freedom mechanical model of orthogonal cutting (a); stability lobe diagram of the cutting process (b); a typical bifurcation scenario (c).

49 Parameter  $\tau$  is the dimensionless regenerative delay or, equivalently, the period of workpiece  
 50 rotation related to the dimensionless angular velocity  $\Omega$  of the workpiece:  $\tau = 2\pi/\Omega$ . Parameter  
 51  $w$  is the dimensionless chip width, whereas  $\eta_2$  and  $\eta_3$  denote dimensionless quadratic and cubic  
 52 cutting-force coefficients related to the prescribed feed per revolution, which is just the unit  
 53 theoretical chip thickness.

54 Equation (2.1) is a delay-differential equation with cubic nonlinearity. The cubic cutting force  
 55 model was introduced in [5]. Note that other cutting force characteristics also exist, see [4] and the  
 56 references therein, but these characteristics can also be approximated by cubic polynomials using  
 57 Taylor series expansion. Approximation of the nonlinearity by a cubic expression is a necessary  
 58 step for the subsequent bifurcation analysis in Sec. 4 and Sec. 5.

59 Equation (2.1) is valid only for positive dimensionless chip thickness,  $h(t) = 1 + x(t - \tau) -$   
 60  $x(t) > 0$ . For large-amplitude vibrations, it might occur that the dimensionless chip thickness  $h(t)$   
 61 drops to zero or to negative values, which indicates that the tool gets out of the workpiece and  
 62 loses contact with the material. In such cases, the cutting force on the right-hand side of (2.1)  
 63 becomes zero irrespective of the tool's position. At this point, we do not investigate loss of contact  
 64 between the tool and the workpiece and assume that  $h(t) > 0$  and (2.1) is valid during the entire  
 65 cutting process.

66 In the rest of the paper, we deal with the stability and bifurcation analysis of (2.1). For  
 67 convenience, the equation is transformed into the first-order form

$$\mathbf{y}'(t) = \mathbf{L}\mathbf{y}(t) + \mathbf{R}\mathbf{y}(t - \tau) + \mathbf{g}(\mathbf{y}_t), \quad (2.2)$$

where  $\mathbf{y}$  is the vector of state variables,  $\mathbf{L}$  and  $\mathbf{R}$  are the coefficient matrices of the linear and the  
 retarded terms, respectively, and  $\mathbf{g}$  contains all nonlinear terms:

$$\mathbf{y}(t) = \begin{bmatrix} x(t) \\ x'(t) \end{bmatrix}, \quad \mathbf{L} = \begin{bmatrix} 0 & 1 \\ -(1+w) & -2\zeta \end{bmatrix}, \quad \mathbf{R} = \begin{bmatrix} 0 & 0 \\ w & 0 \end{bmatrix}, \quad (2.3)$$

$$\mathbf{g}(\mathbf{y}_t) = \begin{bmatrix} 0 \\ w \left( \eta_2 (y_1(t - \tau) - y_1(t))^2 + \eta_3 (y_1(t - \tau) - y_1(t))^3 \right) \end{bmatrix}.$$

68 Here subscript 1 refers to the first component of a vector, i.e.,  $y_1(t) = x(t)$ .

69 Since delay-differential equations have infinite-dimensional phase space [3], the state of the  
 70 system is not determined solely by the vector  $\mathbf{y}(t)$ . Instead, we use a function defined in the  
 71 Banach space  $\mathcal{B}$  of continuously differentiable vector-valued functions to describe the evolution  
 72 of the system: we introduce the shift  $\mathbf{y}_t \in \mathcal{B} : [-\tau, 0] \rightarrow \mathbb{R}^2$ ,  $\mathbf{y}_t(\theta) = \mathbf{y}(t + \theta)$ . Using  $\mathbf{y}_t$ , system (2.1)  
 73 can be represented in operator differential equation (OpDE) form as

$$\mathbf{y}'_t = \mathcal{A}\mathbf{y}_t + \mathcal{F}(\mathbf{y}_t), \quad (2.4)$$

where  $\mathcal{A}, \mathcal{F} : \mathcal{B} \rightarrow \mathcal{B}$  are the linear and the nonlinear operators, respectively, defined by

$$(\mathcal{A}\mathbf{u})(\theta) = \begin{cases} \frac{d}{d\theta}\mathbf{u}(\theta) & \text{if } \theta \in [-\tau, 0), \\ \mathbf{L}\mathbf{u}(0) + \mathbf{R}\mathbf{u}(-\tau) & \text{if } \theta = 0, \end{cases} \quad (2.5)$$

$$(\mathcal{F}(\mathbf{u}))(\theta) = \begin{cases} \mathbf{0} & \text{if } \theta \in [-\tau, 0), \\ \mathbf{g}(\mathbf{u}) & \text{if } \theta = 0. \end{cases} \quad (2.6)$$

### 3. Linear Stability Analysis

Equation (2.1) has a single equilibrium  $x(t) \equiv 0$ , which corresponds to stationary cutting. Machine tool chatter is associated with the loss of stability of this equilibrium. Substitution of the exponential trial solution  $x(t) = Ce^{\lambda t}$ ,  $\lambda, C \in \mathbb{C}$  into (2.1) gives the characteristic function

$$D(\lambda) := \det(\lambda\mathbf{I} - \mathbf{L} - \mathbf{R}e^{-\lambda\tau}) = \lambda^2 + 2\zeta\lambda + 1 + w(1 - e^{-\lambda\tau}). \quad (3.1)$$

Its infinitely many zeros – known as characteristic exponents – are the same as the eigenvalues of the operator  $\mathcal{A}$  in (2.5). The trivial solution is exponentially asymptotically stable if and only if all the characteristic exponents lie in the open left half of the complex plane. The system is at the boundary of stability if a single real root  $\lambda = 0$  or a pair of complex conjugate roots  $\lambda = \pm i\omega$  ( $i^2 = -1$ ,  $\omega > 0$ ) exists, while no characteristic exponents have positive real part. For (3.1), only the latter case with critical roots  $\lambda = \pm i\omega$  is possible, which corresponds to a Hopf bifurcation in the nonlinear system. The analysis of the Hopf bifurcation can be found in [9–11] in details. The Hopf bifurcation points can be located after the separation of  $D(\pm i\omega) = 0$  into real and imaginary parts:

$$\begin{aligned} R(\omega) &= -\omega^2 + 1 + w(1 - \cos(\omega\tau)), \\ S(\omega) &= 2\zeta\omega + w\sin(\omega\tau). \end{aligned} \quad (3.2)$$

Solving  $R(\omega) = 0$  and  $S(\omega) = 0$  gives the linear stability boundaries in the form

$$w_{\text{H}}(\omega) = \frac{(\omega^2 - 1)^2 + 4\zeta^2\omega^2}{2(\omega^2 - 1)}, \quad \tau_{\text{H}}(j, \omega) = \frac{2}{\omega} \left( j\pi - \arctan\left(\frac{\omega^2 - 1}{2\zeta\omega}\right) \right), \quad \Omega_{\text{H}}(j, \omega) = \frac{2\pi}{\tau_{\text{H}}(j, \omega)}, \quad (3.3)$$

where subscript H indicates that (3.3) gives the location of Hopf bifurcation. Note that (3.3) defines a family of curves called stability lobes where  $j \in \mathbb{Z}^+$  is the lobe number. Depicting the stability boundaries in the plane  $(\Omega, w)$  of the technological parameters leads to so-called stability lobe diagrams (see the example in Fig. 1(b) for  $\zeta = 0.02$  where gray shading indicates the linearly stable region associated with chatter-free cutting process).

As it was shown in [9–11], subcritical Hopf bifurcation occurs along the stability lobes. In the vicinity of the stability boundaries, the bifurcation gives rise to an unstable periodic orbit around the linearly stable equilibrium with approximate period  $2\pi/\omega$ . At the intersection points of the stability lobes, a codimension two bifurcation – often referred to as double Hopf bifurcation – takes place. At these points, two pairs of characteristic exponents  $\lambda = \pm i\omega_{1,2}$  lie on the imaginary axis ( $\omega_{1,2} > 0$ ). Let us consider the intersection of the lobes with lobe numbers  $j_1$  and  $j_2$ . The location of this point (the so-called double Hopf point) is given by  $w_{\text{HH}} := w_{\text{H}}(\omega_1) = w_{\text{H}}(\omega_2)$ ,  $\tau_{\text{HH}} := \tau_{\text{H}}(j_1, \omega_1) = \tau_{\text{H}}(j_2, \omega_2)$  and  $\Omega_{\text{HH}} := \Omega_{\text{H}}(j_1, \omega_1) = \Omega_{\text{H}}(j_2, \omega_2)$ , which can be obtained by solving  $R(\omega_1) = 0$ ,  $S(\omega_1) = 0$ ,  $R(\omega_2) = 0$  and  $S(\omega_2) = 0$  numerically for  $\omega_1, \omega_2, w$  and  $\tau$ . Subscript HH refers to Hopf-Hopf (double Hopf) bifurcation.

The rest of the paper deals with the analysis of the double Hopf bifurcation via center manifold reduction and the derivation of the normal form of the resulting four-dimensional center subsystem.

## 106 4. Center Manifold Reduction and Normal Form Calculations

107 In this section, center manifold reduction is used to analyse the long-term dynamics of the time-  
 108 delay system (2.1) in the vicinity of the double Hopf bifurcation point. The theory of center  
 109 manifold reduction is discussed in [3]. The calculation follows the steps of the single Hopf  
 110 bifurcation analysis, which is described in [9–11] in details.

111 At a double Hopf point on the boundary of the linearly stable region, the system has four  
 112 characteristic exponents located on the imaginary axis, while all the other characteristic roots are  
 113 located in the open left half-plane. Therefore, the long-term dynamics of the system is determined  
 114 by the flow on a four-dimensional center manifold, which is embedded in the infinite-dimensional  
 115 phase space of (2.1). This flow can be analysed by decomposing the four-dimensional center  
 116 subsystem (see (4.24) at the end of this Section). In what follows, we perform this decomposition  
 117 using the theorem given by (3.10) and (3.11) in Chap. 7 of [3].

The decomposition theorem of [3] introduces the operator  $\mathcal{A}^*$ , which is formally adjoint to  
 operator  $\mathcal{A}$  relative to a certain bilinear form. The formal adjoint  $\mathcal{A}^* : \mathcal{B}^* \rightarrow \mathcal{B}^*$  must satisfy  
 $(\mathbf{v}, \mathcal{A}\mathbf{u}) = (\mathcal{A}^*\mathbf{v}, \mathbf{u})$  for any pair of  $\mathbf{u} \in \mathcal{B} : [-\tau, 0] \rightarrow \mathbb{R}^2$  and  $\mathbf{v} \in \mathcal{B}^* : [0, \tau] \rightarrow \mathbb{R}^2$ , where  $\mathcal{B}^*$  is the  
 adjoint space and operation  $(\cdot, \cdot) : \mathcal{B}^* \times \mathcal{B} \rightarrow \mathbb{R}$  indicates the bilinear form. The definition of the  
 formal adjoint and the bilinear form can be found in [3] (see (3.1) and (3.3) in Chap. 7), and here  
 they become

$$(\mathcal{A}^*\mathbf{v})(\varphi) = \begin{cases} -\frac{d}{d\varphi}\mathbf{v}(\varphi) & \text{if } \varphi \in (0, \tau], \\ \mathbf{L}^*\mathbf{v}(0) + \mathbf{R}^*\mathbf{v}(\tau) & \text{if } \varphi = 0, \end{cases} \quad (4.1)$$

$$(\mathbf{u}, \mathbf{v}) = \mathbf{u}^*(0)\mathbf{v}(0) + \int_0^\tau \mathbf{u}^*(\varphi)\mathbf{R}\mathbf{v}(\varphi - \tau)d\varphi, \quad (4.2)$$

118 where the superscript  $*$  of  $\mathbf{R}$ ,  $\mathbf{L}$  and  $\mathbf{u}$  refers to conjugate transpose.

### 119 (a) Right and Left Eigenvectors

The four-dimensional center subspace of the associated linear system is tangent to the plane  
 spanned by those infinite-dimensional right eigenvectors (eigenfunctions) of operator  $\mathcal{A}$ , which  
 correspond to the four critical characteristic exponents  $\lambda = \pm i\omega_k$ ,  $k = 1, 2$ . From this point on,  
 index  $k = 1, 2$  is used to indicate that an expression is related to one of the angular frequencies,  
 i.e., either to  $\omega_1$  or to  $\omega_2$ . For  $\tau = \tau_{\text{HH}}$  and  $w = w_{\text{HH}}$ , the four eigenvectors  $\mathbf{s}_k(\theta)$  and  $\bar{\mathbf{s}}_k(\theta)$  satisfy

$$(\mathcal{A}\mathbf{s}_k)(\theta) = i\omega_k\mathbf{s}_k(\theta), \quad (\mathcal{A}\bar{\mathbf{s}}_k)(\theta) = -i\omega_k\bar{\mathbf{s}}_k(\theta), \quad (4.3)$$

where overbar indicates complex conjugate. Decomposing the eigenvectors into real  
 and imaginary parts as  $\mathbf{s}_k(\theta) = \mathbf{s}_{k,\text{R}}(\theta) + i\mathbf{s}_{k,\text{I}}(\theta)$ , substituting  $\tau = \tau_{\text{HH}}$ ,  $w = w_{\text{HH}}$  and the  
 definition (2.5) of operator  $\mathcal{A}$ , we get the boundary value problem

$$\frac{d}{d\theta}\mathbf{s}(\theta) = \mathbf{B}_{8 \times 8}\mathbf{s}(\theta), \quad \theta \in [-\tau_{\text{HH}}, 0], \quad (4.4)$$

$$\mathbf{L}_{8 \times 8}\mathbf{s}(0) + \mathbf{R}_{8 \times 8}\mathbf{s}(-\tau_{\text{HH}}) = \mathbf{B}_{8 \times 8}\mathbf{s}(0). \quad (4.5)$$

The coefficient matrices and  $\mathbf{s}(\theta)$  are defined as

$$\mathbf{s}(\theta) = \begin{bmatrix} \mathbf{s}_{1,\text{R}}(\theta) \\ \mathbf{s}_{1,\text{I}}(\theta) \\ \mathbf{s}_{2,\text{R}}(\theta) \\ \mathbf{s}_{2,\text{I}}(\theta) \end{bmatrix}, \quad \mathbf{B}_{8 \times 8} = \begin{bmatrix} \mathbf{0} & -\omega_1\mathbf{I} & \mathbf{0} & \mathbf{0} \\ \omega_1\mathbf{I} & \mathbf{0} & \mathbf{0} & \mathbf{0} \\ \mathbf{0} & \mathbf{0} & \mathbf{0} & -\omega_2\mathbf{I} \\ \mathbf{0} & \mathbf{0} & \omega_2\mathbf{I} & \mathbf{0} \end{bmatrix}, \quad (4.6)$$

$$\mathbf{L}_{8 \times 8} = \text{diag}[\mathbf{L}, \mathbf{L}, \mathbf{L}, \mathbf{L}]|_{w=w_{\text{HH}}}, \quad \mathbf{R}_{8 \times 8} = \text{diag}[\mathbf{R}, \mathbf{R}, \mathbf{R}, \mathbf{R}]|_{w=w_{\text{HH}}},$$

120 where  $\mathbf{I}$  and  $\mathbf{0}$  denote the  $2 \times 2$  identity and zero matrices, respectively, and  $\text{diag}$  refers to block-  
 121 diagonal matrices. The solution of (4.4) can be written in exponential form as  $\mathbf{s}(\theta) = e^{\mathbf{B}_{8 \times 8}\theta}\mathbf{c}$ . The

constant  $\mathbf{c}$  can be determined from (4.5). In order to select the norm of the right eigenvectors, four components of  $\mathbf{c}$  can be chosen arbitrarily. Now we choose  $c_1 = 1$ ,  $c_3 = 0$ ,  $c_5 = 1$ , and  $c_7 = 0$ , whence we get

$$\mathbf{s}_{k,R}(\theta) = \begin{bmatrix} \cos(\omega_k \theta) \\ -\omega_k \sin(\omega_k \theta) \end{bmatrix}, \quad \mathbf{s}_{k,I}(\theta) = \begin{bmatrix} \sin(\omega_k \theta) \\ \omega_k \cos(\omega_k \theta) \end{bmatrix}. \quad (4.7)$$

The decomposition theorem of [3] also uses the so-called left eigenvectors: the eigenvectors  $\mathbf{n}_k(\varphi)$  and  $\bar{\mathbf{n}}_k(\varphi)$  of the adjoint operator  $\mathcal{A}^*$ . Since the eigenvalues of  $\mathcal{A}^*$  are complex conjugates to those of  $\mathcal{A}$ , the left eigenvectors  $\mathbf{n}_k(\varphi)$  and  $\bar{\mathbf{n}}_k(\varphi)$  satisfy

$$(\mathcal{A}^* \mathbf{n}_k)(\varphi) = -i\omega_k \mathbf{n}_k(\varphi), \quad (\mathcal{A}^* \bar{\mathbf{n}}_k)(\varphi) = i\omega_k \bar{\mathbf{n}}_k(\varphi) \quad (4.8)$$

for  $\tau = \tau_{\text{HH}}$  and  $w = w_{\text{HH}}$ . We decompose the eigenvectors into real and imaginary parts as  $\mathbf{n}_k(\varphi) = \mathbf{n}_{k,R}(\varphi) + i\mathbf{n}_{k,I}(\varphi)$ , where  $\mathbf{n}_{k,R}(\varphi)$  and  $\mathbf{n}_{k,I}(\varphi)$  can be obtained from the boundary value problem defined by (4.8) and (4.1) in the same way as we computed  $\mathbf{s}_{k,R}(\theta)$  and  $\mathbf{s}_{k,I}(\theta)$ . The norm of the left eigenvectors cannot be selected arbitrarily, since they must satisfy the following orthonormality condition in order to apply the decomposition theorem of [3]:

$$(\mathbf{n}_{1,R}, \mathbf{s}_{1,R}) = 1, \quad (\mathbf{n}_{1,R}, \mathbf{s}_{1,I}) = 0, \quad (\mathbf{n}_{2,R}, \mathbf{s}_{2,R}) = 1, \quad (\mathbf{n}_{2,R}, \mathbf{s}_{2,I}) = 0. \quad (4.9)$$

Solving the boundary value problem (4.8) constrained by the orthonormality condition (4.9), we get the left eigenfunctions in the form

$$\mathbf{n}_{k,R}(\varphi) = \frac{2}{p_k^2 + q_k^2} \begin{bmatrix} (2\zeta p_k + \omega_k q_k) \cos(\omega_k \varphi) + (\omega_k p_k - 2\zeta q_k) \sin(\omega_k \varphi) \\ p_k \cos(\omega_k \varphi) - q_k \sin(\omega_k \varphi) \end{bmatrix},$$

$$\mathbf{n}_{k,I}(\varphi) = \frac{2}{p_k^2 + q_k^2} \begin{bmatrix} (-\omega_k p_k + 2\zeta q_k) \cos(\omega_k \varphi) + (2\zeta p_k + \omega_k q_k) \sin(\omega_k \varphi) \\ q_k \cos(\omega_k \varphi) + p_k \sin(\omega_k \varphi) \end{bmatrix}, \quad (4.10)$$

where the constants  $p_k$  and  $q_k$  read

$$p_k = 2\zeta + \tau_{\text{HH}} (1 + w_{\text{HH}} - \omega_k^2), \quad q_k = 2\omega_k (1 + \zeta \tau_{\text{HH}}). \quad (4.11)$$

### (b) Decomposition of the Solution Space

Using the right and left eigenvectors, the four-dimensional center subspace can now be separated via the decomposition theorem given by (3.10) and (3.11) in Chap. 7 of [3]. We decompose the solution as

$$\mathbf{y}_t(\theta) = z_1(t)\mathbf{s}_{1,R}(\theta) + z_2(t)\mathbf{s}_{1,I}(\theta) + z_3(t)\mathbf{s}_{2,R}(\theta) + z_4(t)\mathbf{s}_{2,I}(\theta) + \mathbf{y}_{\text{tn}}(\theta), \quad (4.12)$$

where  $z_1(t)$ ,  $z_2(t)$ ,  $z_3(t)$  and  $z_4(t)$  are local coordinates on the attractive center manifold, which describe the long-term dynamics of the time-delay system (2.1), whereas  $\mathbf{y}_{\text{tn}}(\theta)$  accounts for the remaining infinite-dimensional stable subsystem with coordinates transverse to the center manifold. The decomposition theorem gives the formula of these components:

$$z_1(t) = (\mathbf{n}_{1,R}, \mathbf{y}_t), \quad z_2(t) = (\mathbf{n}_{1,I}, \mathbf{y}_t), \quad z_3(t) = (\mathbf{n}_{2,R}, \mathbf{y}_t), \quad z_4(t) = (\mathbf{n}_{2,I}, \mathbf{y}_t),$$

$$\mathbf{y}_{\text{tn}}(\theta) = \mathbf{y}_t(\theta) - z_1(t)\mathbf{s}_{1,R}(\theta) - z_2(t)\mathbf{s}_{1,I}(\theta) - z_3(t)\mathbf{s}_{2,R}(\theta) - z_4(t)\mathbf{s}_{2,I}(\theta). \quad (4.13)$$

From this point on, we omit the argument  $t$  from  $z_1$ ,  $z_2$ ,  $z_3$  and  $z_4$  for the sake of simplicity. Differentiating (4.13) with respect to time and using (2.4), (4.12) and (4.3), we get

$$\begin{bmatrix} z_1' \\ z_2' \\ z_3' \\ z_4' \\ \mathbf{y}_{\text{tn}}' \end{bmatrix} = \begin{bmatrix} 0 & \omega_1 & 0 & 0 & \mathcal{O} \\ -\omega_1 & 0 & 0 & 0 & \mathcal{O} \\ 0 & 0 & 0 & \omega_2 & \mathcal{O} \\ 0 & 0 & -\omega_2 & 0 & \mathcal{O} \\ \mathbf{0} & \mathbf{0} & \mathbf{0} & \mathbf{0} & \mathcal{A} \end{bmatrix} \begin{bmatrix} z_1 \\ z_2 \\ z_3 \\ z_4 \\ \mathbf{y}_{\text{tn}} \end{bmatrix} + \begin{bmatrix} n_{1,R,2}(0)\mathcal{F}_2(0) \\ n_{1,I,2}(0)\mathcal{F}_2(0) \\ n_{2,R,2}(0)\mathcal{F}_2(0) \\ n_{2,I,2}(0)\mathcal{F}_2(0) \\ \mathcal{G}(\mathbf{y}_t) \end{bmatrix}, \quad (4.14)$$

$$\mathcal{G}(\mathbf{y}_t) = \mathcal{F}(\mathbf{y}_t) - \mathcal{F}_2(0) (n_{1,R,2}(0)\mathbf{s}_{1,R} + n_{1,I,2}(0)\mathbf{s}_{1,I} + n_{2,R,2}(0)\mathbf{s}_{2,R} + n_{2,I,2}(0)\mathbf{s}_{2,I}),$$

140 where  $\mathfrak{o} : \mathbb{R} \rightarrow \mathcal{B}$  is a zero operator,  $\mathcal{O} : \mathcal{B} \rightarrow \mathbb{R}$  is a zero functional, subscript 2 in  $n_{k,R,2}$  and  $n_{k,I,2}$   
 141 indicates the second component of vectors, and  $\mathcal{F}_2(0)$  shortly indicates the second component of  
 142  $\mathcal{F}(\mathbf{y}_t)$  at  $\theta = 0$  with  $\tau = \tau_{HH}$  and  $w = w_{HH}$ .

### 143 (c) Approximation of the Center Manifold

144 Equation (4.14) shows that the four-dimensional center subsystem is decoupled in the associated  
 145 linear system, but there is still coupling in the nonlinear terms. In order to fully decouple the four-  
 146 dimensional subsystem, the dynamics must be restricted to the center manifold of form  $\mathbf{y}_{tn} =$   
 147  $\mathbf{y}_{tn}^{CM}(z_1, z_2, z_3, z_4)$ . The nonlinear terms in the first four rows of (4.14) must be expanded into  
 148 Taylor series in terms of  $z_1, z_2, z_3$  and  $z_4$  in order to do normal form analysis – we must expand  
 149  $\mathcal{F}_2(0)$  up to third order. The computation of the center manifold and the Taylor expansion is rather  
 150 lengthy, but it can be tackled by symbolic algebra. Now we present the milestones of this process.

151 Substituting the decomposed solution (4.12) into the definition (2.6) of  $\mathcal{F}$ , we get the Taylor  
 152 series expansion of  $\mathcal{F}_2(0)$  if the center manifold  $\mathbf{y}_{tn} = \mathbf{y}_{tn}^{CM}(z_1, z_2, z_3, z_4)$  is expanded into Taylor  
 153 series in terms of  $z_{1,2,3,4}$ . The second-order terms in  $\mathcal{F}_2(0)$  are independent of  $\mathbf{y}_{tn}^{CM}$ , the expansion  
 154 of the center manifold is necessary only to obtain the cubic (and higher-order) terms in  $\mathcal{F}_2(0)$ . The  
 155 quadratic part of  $\mathcal{F}_2(0)$  is of form

$$\begin{aligned} \mathcal{F}_2^{2nd}(0) = & F_{11}z_1^2 + F_{22}z_2^2 + F_{33}z_3^2 + F_{44}z_4^2 \\ & + F_{12}z_1z_2 + F_{13}z_1z_3 + F_{14}z_1z_4 + F_{23}z_2z_3 + F_{24}z_2z_4 + F_{34}z_3z_4, \end{aligned} \quad (4.15)$$

$$F_{mn} = \frac{1}{2} \left. \frac{\partial^2 \mathcal{F}_2(0)}{\partial z_m^2} \right|_0, \quad \text{if } m = n, \quad F_{mn} = \left. \frac{\partial^2 \mathcal{F}_2(0)}{\partial z_m \partial z_n} \right|_0, \quad \text{if } m < n,$$

$m, n = 1, 2, 3, 4$ , where the subscript  $\mathbf{0}$  stands for the substitution  $\mathbf{y}_t(0) = \mathbf{0}$ . In order to include all  
 cubic terms in  $\mathcal{F}_2(0)$ , we need at least the second-order expansion of the center manifold  $\mathbf{y}_{tn}^{CM}$  in  
 terms of  $z_{1,2,3,4}$ :

$$\begin{aligned} \mathbf{y}_{tn}^{CM}(z_1, z_2, z_3, z_4)(\theta) \approx & \frac{1}{2} \left( \mathbf{h}_{11}(\theta)z_1^2 + \mathbf{h}_{22}(\theta)z_2^2 + \mathbf{h}_{33}(\theta)z_3^2 + \mathbf{h}_{44}(\theta)z_4^2 \right. \\ & \left. + 2\mathbf{h}_{12}(\theta)z_1z_2 + 2\mathbf{h}_{13}(\theta)z_1z_3 + 2\mathbf{h}_{14}(\theta)z_1z_4 + 2\mathbf{h}_{23}(\theta)z_2z_3 + 2\mathbf{h}_{24}(\theta)z_2z_4 + 2\mathbf{h}_{34}(\theta)z_3z_4 \right). \end{aligned} \quad (4.16)$$

The coefficients  $\mathbf{h}_{mn}(\theta)$  ( $m, n = 1, 2, 3, 4, m \leq n$ ) can be determined as follows. Both sides  
 of (4.16) are differentiated with respect to time, then the first four rows of (4.14) are substituted  
 into the right-hand side and the fifth row of (4.14) is substituted into the left-hand side. The  
 case  $\theta \in [-\tau_{HH}, 0)$  is considered and the definitions (2.5)-(2.6) of  $\mathcal{A}$  and  $\mathcal{F}$  are substituted  
 accordingly. Afterwards, the derivative of (4.16) with respect to  $\theta$  is substituted and the second-  
 order approximation  $\mathcal{F}_2(0) \approx \mathcal{F}_2^{2nd}(0)$  is used. Finally, the coefficients of the quadratic terms of  
 $z_{1,2,3,4}$  are collected and a polynomial balance is considered. This leads to three decoupled sets  
 of non-homogeneous first-order differential equations:

$$\frac{d}{d\theta} \mathbf{H}_l(\theta) = \mathbf{C}_l \mathbf{H}_l(\theta) + \mathbf{p}_{1,l} \cos(\omega_1 \theta) + \mathbf{q}_{1,l} \sin(\omega_1 \theta) + \mathbf{p}_{2,l} \cos(\omega_2 \theta) + \mathbf{q}_{2,l} \sin(\omega_2 \theta), \quad (4.17)$$

156  $l = 1, 2, 3$ , where

$$\mathbf{H}_1(\theta) = \begin{bmatrix} \mathbf{h}_{11}(\theta) \\ \mathbf{h}_{12}(\theta) \\ \mathbf{h}_{22}(\theta) \end{bmatrix}, \quad \mathbf{H}_2(\theta) = \begin{bmatrix} \mathbf{h}_{33}(\theta) \\ \mathbf{h}_{34}(\theta) \\ \mathbf{h}_{44}(\theta) \end{bmatrix}, \quad \mathbf{H}_3(\theta) = \begin{bmatrix} \mathbf{h}_{13}(\theta) \\ \mathbf{h}_{14}(\theta) \\ \mathbf{h}_{23}(\theta) \\ \mathbf{h}_{24}(\theta) \end{bmatrix}, \quad \mathbf{Q}_k = \frac{2}{p_k^2 + q_k^2} \begin{bmatrix} p_k & q_k \\ q_k \omega_k & -p_k \omega_k \end{bmatrix},$$

$$\begin{bmatrix} \mathbf{p}_{k,1} & \mathbf{q}_{k,1} \end{bmatrix} = \begin{bmatrix} 2F_{11} \mathbf{Q}_k \\ F_{12} \mathbf{Q}_k \\ 2F_{22} \mathbf{Q}_k \end{bmatrix}, \quad \begin{bmatrix} \mathbf{p}_{k,2} & \mathbf{q}_{k,2} \end{bmatrix} = \begin{bmatrix} 2F_{33} \mathbf{Q}_k \\ F_{34} \mathbf{Q}_k \\ 2F_{44} \mathbf{Q}_k \end{bmatrix}, \quad \begin{bmatrix} \mathbf{p}_{k,3} & \mathbf{q}_{k,3} \end{bmatrix} = \begin{bmatrix} F_{13} \mathbf{Q}_k \\ F_{14} \mathbf{Q}_k \\ F_{23} \mathbf{Q}_k \\ F_{24} \mathbf{Q}_k \end{bmatrix},$$

$$\mathbf{C}_k = \begin{bmatrix} \mathbf{0} & -2\omega_k \mathbf{I} & \mathbf{0} \\ \omega_k \mathbf{I} & \mathbf{0} & -\omega_k \mathbf{I} \\ \mathbf{0} & 2\omega_k \mathbf{I} & \mathbf{0} \end{bmatrix}, \quad \mathbf{C}_3 = \begin{bmatrix} \mathbf{0} & -\omega_2 \mathbf{I} & -\omega_1 \mathbf{I} & \mathbf{0} \\ \omega_2 \mathbf{I} & \mathbf{0} & \mathbf{0} & -\omega_1 \mathbf{I} \\ \omega_1 \mathbf{I} & \mathbf{0} & \mathbf{0} & -\omega_2 \mathbf{I} \\ \mathbf{0} & \omega_1 \mathbf{I} & \omega_2 \mathbf{I} & \mathbf{0} \end{bmatrix}.$$

(4.18)

157 The solution of (4.17) takes the form

$$\mathbf{H}_l(\theta) = e^{\mathbf{C}_l \theta} \mathbf{K}_l + \mathbf{M}_{1,l} \cos(\omega_1 \theta) + \mathbf{N}_{1,l} \sin(\omega_1 \theta) + \mathbf{M}_{2,l} \cos(\omega_2 \theta) + \mathbf{N}_{2,l} \sin(\omega_2 \theta), \quad (4.19)$$

158  $l = 1, 2, 3$ . The coefficients  $\mathbf{M}_{k,l}$  and  $\mathbf{N}_{k,l}$  can be determined by substituting (4.19) back into (4.17)  
159 and considering the harmonic balance of the trigonometric terms, which yields

$$\begin{bmatrix} \mathbf{M}_{k,l} \\ \mathbf{N}_{k,l} \end{bmatrix} = \begin{bmatrix} -\mathbf{C}_l & \omega_k \mathbf{I} \\ -\omega_k \mathbf{I} & -\mathbf{C}_l \end{bmatrix}^{-1} \begin{bmatrix} \mathbf{p}_{k,l} \\ \mathbf{q}_{k,l} \end{bmatrix}. \quad (4.20)$$

160 In order to determine the coefficient  $\mathbf{K}_l$  in (4.19), a boundary condition corresponding to (4.17)  
161 must be derived and satisfied. The boundary condition is formulated similarly as the differential  
162 equation (4.17). Both sides of (4.16) are differentiated with respect to time, then the first four rows  
163 of (4.14) are substituted into the right-hand side and the fifth row of (4.14) is substituted into the  
164 left-hand side as before. Now the case  $\theta = 0$  is considered when using the definitions (2.5)-(2.6) of  
165  $\mathcal{A}$  and  $\mathcal{F}$ . Afterwards, (4.16) is substituted and the second-order approximation  $\mathcal{F}_2(0) \approx \mathcal{F}_2^{\text{2nd}}(0)$   
166 is used. The coefficients of the quadratic terms of  $z_{1,2,3,4}$  are collected for a polynomial balance  
167 and, by taking  $\tau = \tau_{\text{HH}}$ ,  $w = w_{\text{HH}}$ , it leads to the boundary conditions for (4.17) in the form

$$\mathbf{P}_l \mathbf{H}_l(0) + \mathbf{R}_l \mathbf{H}_l(-\tau_{\text{HH}}) = \mathbf{p}_{1,l} + \mathbf{p}_{2,l} + \mathbf{r}_l, \quad (4.21)$$

where

$$\mathbf{L}_k = \mathbf{L}_{6 \times 6} = \text{diag}[\mathbf{L}, \mathbf{L}, \mathbf{L}]|_{w=w_{\text{HH}}}, \quad \mathbf{L}_3 = \mathbf{L}_{8 \times 8}, \quad \mathbf{P}_l = \mathbf{L}_l - \mathbf{C}_l,$$

$$\mathbf{R}_k = \mathbf{R}_{6 \times 6} = \text{diag}[\mathbf{R}, \mathbf{R}, \mathbf{R}]|_{w=w_{\text{HH}}}, \quad \mathbf{R}_3 = \mathbf{R}_{8 \times 8},$$

$$\mathbf{r}_1 = - \begin{bmatrix} 0 & 2F_{11} & 0 & F_{12} & 0 & 2F_{22} \end{bmatrix}^T, \quad (4.22)$$

$$\mathbf{r}_2 = - \begin{bmatrix} 0 & 2F_{33} & 0 & F_{34} & 0 & 2F_{44} \end{bmatrix}^T,$$

$$\mathbf{r}_3 = - \begin{bmatrix} 0 & F_{13} & 0 & F_{14} & 0 & F_{23} & 0 & F_{24} \end{bmatrix}^T.$$

168 Finally, substituting the trial solution (4.19) into the boundary condition (4.21), we obtain the  
169 coefficient  $\mathbf{K}_l$ . After some simplifications, we can write  $\mathbf{K}_l$  in the form

$$\mathbf{K}_l = \left( \mathbf{P}_l + \mathbf{R}_l e^{-\mathbf{C}_l \tau} \right)^{-1} \mathbf{r}_l. \quad (4.23)$$

170 This way, the solution (4.19) of the above boundary value problem is constructed and the  
171 coefficients  $\mathbf{h}_{mn}(\theta)$  ( $m, n = 1, 2, 3, 4, m \leq n$ ) are available. The second-order approximation (4.16)  
172 of the center manifold is obtained and, with (4.12), it can be used to derive the third-order



173 expansion of  $\mathcal{F}_2(0)$  in terms of  $z_{1,2,3,4}$ . Thus, the nonlinearity in the first four rows of (4.14)  
 174 is now expressed in terms of the four local coordinates of the center manifold, and we get a  
 175 four-dimensional subsystem with cubic nonlinearity in the form

$$\begin{bmatrix} z_1' \\ z_2' \\ z_3' \\ z_4' \end{bmatrix} = \begin{bmatrix} 0 & \omega_1 & 0 & 0 \\ -\omega_1 & 0 & 0 & 0 \\ 0 & 0 & 0 & \omega_2 \\ 0 & 0 & -\omega_2 & 0 \end{bmatrix} \begin{bmatrix} z_1 \\ z_2 \\ z_3 \\ z_4 \end{bmatrix} + \begin{bmatrix} G_1(z_1, z_2, z_3, z_4) \\ G_2(z_1, z_2, z_3, z_4) \\ G_3(z_1, z_2, z_3, z_4) \\ G_4(z_1, z_2, z_3, z_4) \end{bmatrix}. \quad (4.24)$$

176 The lengthy process of center manifold reduction has been performed in order to decouple  
 177 the four-dimensional center subsystem (4.24). The advantage of this formulation is that the long-  
 178 term dynamics of the original infinite-dimensional time-delay system (2.1) can be investigated by  
 179 analysing the finite-dimensional ordinary differential equation (4.24). Hence, from this point on,  
 180 the bifurcation theorems and normal forms of ordinary differential equations can be used, which  
 181 are well-known in the literature [17,19]. In the next section, we use normal form theory to analyse  
 182 the flow on the center manifold and show the existence of periodic and quasi-periodic motions.

### 183 (d) Normal Form Equations

The four-dimensional system (4.24) can be transformed into polar form with two amplitudes  $r_1$ ,  
 $r_2$  and two phase angles  $\theta_1, \theta_2$  as

$$\begin{aligned} r_1' &= \mu_1 r_1 + a_{11} r_1^3 + a_{12} r_1 r_2^2, & \theta_1' &= \omega_1 + c_{11} r_1^2 + c_{12} r_2^2, \\ r_2' &= \mu_2 r_2 + a_{21} r_1^2 r_2 + a_{22} r_2^3, & \theta_2' &= \omega_2 + c_{21} r_1^2 + c_{22} r_2^2. \end{aligned} \quad (4.25)$$

184 Now we focus on the amplitudes  $r_1, r_2$  only and investigate the existence of periodic and quasi-  
 185 periodic solutions by giving analytical formulae for coefficients  $\mu_1, \mu_2$ , and  $a_{11}, a_{12}, a_{21}, a_{22}$ .

186 The coefficients  $\mu_1, \mu_2$  of the linear terms in (4.25) are unfolding parameters that are functions  
 187 of the bifurcation parameters. The double Hopf bifurcation is a codimension two bifurcation,  
 188 hence two bifurcation parameters must be selected. Now we choose the dimensionless chip  
 189 width  $w$  and the dimensionless angular velocity  $\Omega$ . For convenience, we introduce the shifted  
 190 parameters  $\hat{w} = w - w_{\text{HH}}$  and  $\hat{\Omega} = \Omega - \Omega_{\text{HH}}$  to investigate the system in the vicinity of the  
 191 double Hopf bifurcation. We can approximate the unfolding parameters by linear functions of  
 192 the bifurcation parameters as

$$\begin{aligned} \mu_1 &= \gamma_{11} \hat{w} + \gamma_{12} \hat{\Omega}, \\ \mu_2 &= \gamma_{21} \hat{w} + \gamma_{22} \hat{\Omega}, \end{aligned} \quad (4.26)$$

where the constants  $\gamma_{mn}$  ( $m, n = 1, 2$ ) are called the root tendencies. The constants  $\gamma_{mn}$  represent  
 the speed by which the four critical characteristic exponents cross the imaginary axis during the  
 double Hopf bifurcation. They can be obtained via implicit differentiation of the characteristic  
 equation  $D(\lambda) = 0$ . Using (3.1), this yields

$$\begin{aligned} \gamma_{k1} &= \text{Re} \left( \frac{\partial \lambda}{\partial w} \Big|_{\lambda=i\omega_k} \right) = \text{Re} \left( - \frac{\frac{\partial D}{\partial w}}{\frac{\partial D}{\partial \lambda}} \Big|_{\lambda=i\omega_k} \right) = \frac{p_k V_k + q_k W_k}{p_k^2 + q_k^2}, \\ \gamma_{k2} &= \text{Re} \left( \frac{\partial \lambda}{\partial \Omega} \Big|_{\lambda=i\omega_k} \right) = \text{Re} \left( - \frac{\frac{\partial D}{\partial \tau} \frac{d\tau}{d\Omega}}{\frac{\partial D}{\partial \lambda}} \Big|_{\lambda=i\omega_k} \right) = w_{\text{HH}} \frac{\tau_{\text{HH}}^2}{2\pi} \omega_k \frac{q_k (V_k + 1) - p_k W_k}{p_k^2 + q_k^2}, \end{aligned} \quad (4.27)$$

193 where  $p_k$  and  $q_k$  are defined by (4.11), whereas  $V_k$  and  $W_k$  are given by

$$V_k = \cos(\omega_k \tau_{\text{HH}}) - 1, \quad W_k = -\sin(\omega_k \tau_{\text{HH}}). \quad (4.28)$$

The coefficients  $a_{mn}$  ( $m, n = 1, 2$ ) of the cubic terms in (4.25) can be obtained from the results  
 of center manifold reduction. These normal form coefficients can directly be calculated from the

nonlinear terms of (4.24) by applying the formulae derived in [43], whence we obtain

$$\begin{aligned}
 a_{11} &= -\frac{1}{2}w^2(V_1^2 + W_1^2)\eta_2^2 \left( \frac{K_1R_1 + L_1S_1}{K_1^2 + L_1^2} \frac{p_1V_1 + q_1W_1}{p_1^2 + q_1^2} + \frac{K_1S_1 - L_1R_1}{K_1^2 + L_1^2} \frac{q_1V_1 - p_1W_1}{p_1^2 + q_1^2} \right) \\
 &\quad + \frac{3}{4}w(V_1^2 + W_1^2)\eta_3 \frac{p_1V_1 + q_1W_1}{p_1^2 + q_1^2}, \\
 a_{12} &= -w^2(V_2^2 + W_2^2)\eta_2^2 \left( \left( \frac{K_3R_3 + L_3S_3}{K_3^2 + L_3^2} + \frac{K_4R_4 + L_4S_4}{K_4^2 + L_4^2} \right) \frac{p_1V_1 + q_1W_1}{p_1^2 + q_1^2} \right. \\
 &\quad \left. + \left( \frac{K_3S_3 - L_3R_3}{K_3^2 + L_3^2} - \frac{K_4S_4 - L_4R_4}{K_4^2 + L_4^2} \right) \frac{q_1V_1 - p_1W_1}{p_1^2 + q_1^2} \right) + \frac{3}{2}w(V_2^2 + W_2^2)\eta_3 \frac{p_1V_1 + q_1W_1}{p_1^2 + q_1^2},
 \end{aligned}
 \tag{4.29}$$

194 where  $\eta_2$  and  $\eta_3$  are the cutting force coefficients that appear in (2.1), while the auxiliary  
 195 parameters are

$$\begin{aligned}
 R_k &= 1 - \cos(2\omega_k\tau_{HH}), & S_k &= \sin(2\omega_k\tau_{HH}), \\
 R_{3,4} &= 1 - \cos((\omega_2 \pm \omega_1)\tau_{HH}), & S_{3,4} &= \sin((\omega_2 \pm \omega_1)\tau_{HH}), \\
 K_k &= wR_k - (4\omega_k^2 - 1), & L_k &= wS_k + 4\zeta\omega_k, \\
 K_{3,4} &= wR_{3,4} - ((\omega_2 \pm \omega_1)^2 - 1), & L_{3,4} &= wS_{3,4} + 2\zeta(\omega_2 \pm \omega_1).
 \end{aligned}
 \tag{4.30}$$

196 The expressions of  $a_{22}$  and  $a_{21}$  are the same as that of  $a_{11}$  and  $a_{12}$ , respectively, but the roles of  
 197  $\omega_1$  and  $\omega_2$  are interchanged. The formula of  $a_{22}$  can be obtained from that of  $a_{11}$  by replacing  $K_1$ ,  
 198  $L_1$ ,  $p_1$ ,  $q_1$ ,  $V_1$ ,  $W_1$ ,  $R_1$  and  $S_1$  with  $K_2$ ,  $L_2$ ,  $p_2$ ,  $q_2$ ,  $V_2$ ,  $W_2$ ,  $R_2$  and  $S_2$ , respectively. Whereas the  
 199 formula of  $a_{21}$  is the same as that of  $a_{12}$  but with  $p_2$ ,  $q_2$ ,  $V_2$ ,  $W_2$ ,  $V_1$ , and  $W_1$  instead of  $p_1$ ,  $q_1$ ,  
 200  $V_1$ ,  $W_1$ ,  $V_2$ , and  $W_2$ , respectively, and replacing  $L_4$ ,  $S_4$  with  $-L_4$ ,  $-S_4$  (see the change of the sign  
 201 when interchanging  $\omega_1$  and  $\omega_2$  in the definition (4.30) of  $L_4$  and  $S_4$ ).

202 The above formulae are valid for non-resonant double Hopf bifurcation, where the angular  
 203 frequencies  $\omega_1$  and  $\omega_2$  are not related by small integer numbers. Note that for specific values  
 204 of the damping ratio  $\zeta$ , it might be possible to obtain weak resonant double Hopf bifurcations  
 205 [44], but their analysis is out of scope of this paper. The formula (4.29) of  $a_{11}$  is the same as  
 206 that obtained for the Poincaré-Lyapunov constant via the analysis of the single Hopf bifurcation  
 207 in [11]. It is also important to note that the cubic coefficients  $a_{mn}$  ( $m, n = 1, 2$ ) are in fact functions  
 208 of the bifurcation parameters  $w$  and  $\Omega$ , and (4.29) gives only their constant approximation. In  
 209 Sec. 5, we show a linear approximation of the cubic coefficients  $a_{mn}$  in terms of the bifurcation  
 210 parameters  $w$  and  $\Omega$  following [45]. The linear approximation leads to a higher-order estimation  
 211 of the amplitude of the arising periodic and quasi-periodic motions.

## 212 5. Stability Charts and Bifurcation Diagrams

The analysis of the polar-form system (4.25) can be found in [17]. Accordingly, (4.25) can be further  
 simplified by the transformation  $r_1 = \bar{r}_1/\sqrt{|a_{11}|}$ ,  $r_2 = \bar{r}_2/\sqrt{|a_{22}|}$ :

$$\begin{aligned}
 \bar{r}'_1 &= \bar{r}_1 \left( \mu_1 + a\bar{r}_1^2 + b\bar{r}_2^2 \right), \\
 \bar{r}'_2 &= \bar{r}_2 \left( \mu_2 + c\bar{r}_1^2 + d\bar{r}_2^2 \right),
 \end{aligned}
 \tag{5.1}$$

213 where  $a = a_{11}/|a_{11}|$ ,  $b = a_{12}/|a_{22}|$ ,  $c = a_{21}/|a_{11}|$  and  $d = a_{22}/|a_{22}|$ . These four parameters are  
 214 important, since they determine the possible topologies in the phase portraits of the polar-form  
 215 system (4.25). Simplified phase portraits can be depicted in the plane  $(r_1, r_2)$  for different values of  
 216 the bifurcation parameters  $w$  and  $\Omega$ . As it was shown in [17], the topology of these phase portraits  
 217 depends on the signs of  $a, b, c, d$  and  $A = ad - bc$ . Depending on their signs, twelve different cases  
 218 of unfolding (twelve sets of different topologies) can occur (see pages 399–409 in [17]). For (2.1),  
 219 the Hopf bifurcation is always subcritical [11], thus  $a > 0$  and  $d > 0$  hold, which excludes some of  
 220 these twelve cases. As it is shown below, two of the twelve topologies can be identified.

**Table 1.** The parameters of the double Hopf bifurcation points shown in Fig. 2.

| $j_1$ | $j_2$ | $\omega_1$ | $\omega_2$ | $\Omega_{HH}$ | $w_{HH}$ | $\gamma_{11}$ | $\gamma_{12}$ | $\gamma_{21}$ | $\gamma_{22}$ |
|-------|-------|------------|------------|---------------|----------|---------------|---------------|---------------|---------------|
| 1     | 2     | 1.0006     | 1.52994    | 1.01018       | 0.671754 | 0.005553      | 0.3623        | 0.2963        | -0.6699       |
| 4     | 5     | 1.00247    | 1.15031    | 0.253092      | 0.164877 | 0.02429       | 1.251         | 0.3182        | -1.530        |

**Table 2.** The cubic coefficients of the double Hopf bifurcation points shown in Fig. 2.

| $j_1$ | $j_2$ | $a_{11}$               | $a_{12}$ | $a_{21}$  | $a_{22}$ | $a$ | $b$     | $c$   | $d$ | $A$    |
|-------|-------|------------------------|----------|-----------|----------|-----|---------|-------|-----|--------|
| 1     | 2     | $8.090 \times 10^{-6}$ | 0.008128 | 0.0002925 | 0.4317   | 1   | 0.01883 | 36.16 | 1   | 0.3193 |
| 4     | 5     | $1.460 \times 10^{-4}$ | 0.01560  | 0.002356  | 0.1121   | 1   | 0.1392  | 16.14 | 1   | -1.248 |

### 221 (a) Phase Portraits and Topologies

222 Here we show a numerical case study for damping ratio  $\zeta = 0.02$  and cutting-force coefficients  
 223  $\eta_2 = 1.43059$  and  $\eta_3 = 0.738487$ , which are the dimensionless counterparts of actual measured  
 224 cutting-force coefficients reported in [5] with feed  $h_0 = 250 \mu\text{m}$  per revolution. We found that  
 225 topology Case Ia of [17] occurs at the intersection of the first and the second stability lobes, while  
 226 the intersections of higher-order lobes are all associated with Case Ib of [17]. In what follows, we  
 227 demonstrate the differences between the two cases.

228 Consider the intersection of the first ( $j_1 = 1$ ) and the second ( $j_2 = 2$ ) stability lobes, which is  
 229 marked by a circle in Fig. 1(b) and is also shown by thick lines in more detail in Fig. 2(a). The  
 230 first row of Tab. 1 presents the location  $(\Omega_{HH}, w_{HH})$  of the intersection point, the two angular  
 231 frequencies  $\omega_1, \omega_2$  and the root tendencies  $\gamma_{mn}$  ( $m, n = 1, 2$ ). The cubic coefficients  $a_{mn}$  ( $m, n =$   
 232  $1, 2$ ) and parameters  $a, b, c, d$  and  $A$  are listed in the first row of Tab. 2. In this example,  $a, b, c, d$   
 233 and  $A$  are all positive, which corresponds to Case Ia in [17]. We also computed coefficients  $b$  and  
 234  $c$  numerically by DDE-BIFTOOL [40] and obtained the same results up to the displayed digits.

The corresponding phase portraits and their topologies are shown in Fig. 2(a). According  
 to [17], six different topologies can be distinguished for Case Ia depending on the unfolding  
 parameters  $\mu_1$  and  $\mu_2$ . Correspondingly, six sectors with different topologies can be separated  
 in the plane  $(\Omega, w)$  of the bifurcation parameters. The straight lines separating these sectors are

$$\begin{aligned}
 \text{Line 1: } \mu_1 = 0 & \Rightarrow \hat{w} = -\frac{\gamma_{12}}{\gamma_{11}} \hat{\Omega}, \\
 \text{Line 2: } \mu_2 = 0 & \Rightarrow \hat{w} = -\frac{\gamma_{22}}{\gamma_{21}} \hat{\Omega}, \\
 \text{Line 3: } \mu_2 = \frac{c}{a} \mu_1 & \Rightarrow \hat{w} = \frac{c\gamma_{12} - a\gamma_{22}}{a\gamma_{21} - c\gamma_{11}} \hat{\Omega}, \\
 \text{Line 4: } \mu_2 = \frac{d}{b} \mu_1 & \Rightarrow \hat{w} = \frac{d\gamma_{12} - b\gamma_{22}}{b\gamma_{21} - d\gamma_{11}} \hat{\Omega}.
 \end{aligned} \tag{5.2}$$

235 Note that Lines 1 and 2 are the tangents of the intersecting stability lobes at the double Hopf point  
 236 (the lobes are shown by thick blue and cyan lines in Fig. 2).

237 Let us investigate the sectors of plane  $(\mu_1, \mu_2)$  by going around anti-clockwise. In Sector I  
 238 ( $\mu_1 > 0, \mu_2 > 0$ ), (4.25) has only a single, trivial equilibrium  $(r_1, r_2) = (0, 0)$ , which corresponds  
 239 to the trivial equilibrium of the original time-delay system (2.1) and exists in all the six sectors.  
 240 The trivial equilibrium  $(0, 0)$  is a source (unstable node) in Sector I. The equilibrium undergoes a  
 241 pitchfork bifurcation while crossing Line 1, which gives rise to a non-trivial equilibrium  $(r_1, r_2) =$   
 242  $(r_1^P, 0)$ ,  $r_1^P \neq 0$  in Sector II ( $\mu_1 < 0, \mu_2 > 0$ ). This equilibrium corresponds to a periodic solution  
 243 ( $P_1$ ) in the time-delay system (2.1), whereas the pitchfork bifurcation in system (4.25) corresponds  
 244 to a Hopf bifurcation in the delay-differential equation (2.1). In Sector II, the equilibrium  $(r_1^P, 0)$   
 245 is a source, therefore the corresponding periodic solution  $P_1$  is unstable, while the trivial

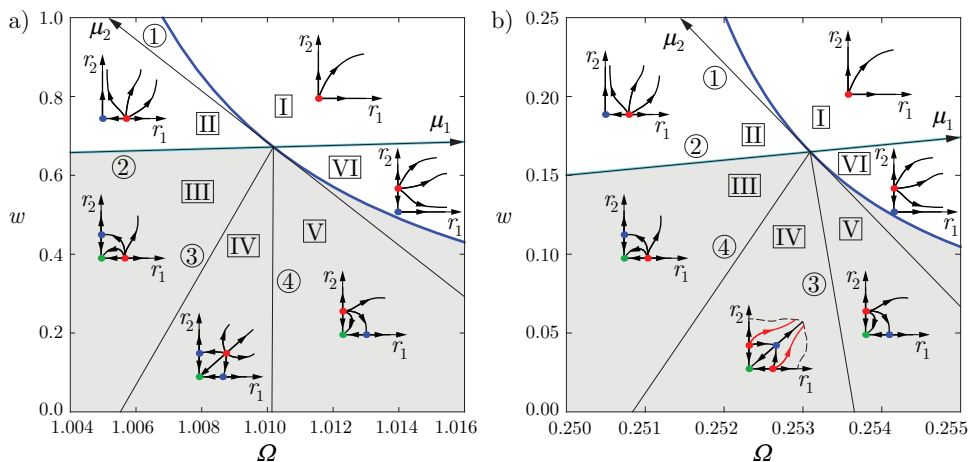


**Figure 2.** The possible phase portrait topologies in the vicinity of the double Hopf bifurcation at the intersection of the first and the second lobes (a); at the intersection of the fourth and the fifth lobes (b). The intersecting stability lobes are shown by thick blue and cyan lines. Sources, sinks and saddles are indicated by red, green and blue dots, respectively.

246 equilibrium  $(0, 0)$  becomes a saddle. Another pitchfork bifurcation of  $(0, 0)$  takes place along Line  
 247 2, and a non-trivial equilibrium  $(r_1, r_2) = (0, r_2^P)$ ,  $r_2^P \neq 0$  is born when entering Sector III ( $\mu_1 < 0$ ,  
 248  $c\mu_1/a < \mu_2 < 0$ ). This, again, corresponds to a Hopf bifurcation of the equilibrium of the infinite-  
 249 dimensional time-delay system (2.1), which gives rise to another periodic solution ( $P_2$ ). In Sector  
 250 III, the trivial equilibrium becomes a sink (stable node), the equilibrium  $(r_1^P, 0)$  remains a source  
 251 and the equilibrium  $(0, r_2^P)$  is a saddle. When entering Sector IV ( $\mu_1 < 0$ ,  $d\mu_1/b < \mu_2 < c\mu_1/a$ ),  
 252 a pitchfork bifurcation of  $(r_1^P, 0)$  gives rise to the non-trivial equilibrium  $(r_1, r_2) = (r_1^{QP}, r_2^{QP})$ ,  
 253  $r_1^{QP} \neq 0$ ,  $r_2^{QP} \neq 0$ . This phenomenon corresponds to a torus bifurcation of the periodic solution  $P_1$   
 254 of (2.1), by which a quasi-periodic solution (QP) arises. Thus, in Sector IV, the trivial equilibrium  
 255 coexists with two periodic solutions and a quasi-periodic one. The trivial equilibrium is still a sink,  
 256 the equilibrium  $(0, r_2^P)$  is still a saddle, while the equilibrium  $(r_1^P, 0)$  becomes a saddle and the  
 257 equilibrium  $(r_1^{QP}, r_2^{QP})$  is born as a source. The equilibrium  $(r_1^{QP}, r_2^{QP})$  merges with the equilibrium  
 258  $(0, r_2^P)$  via a pitchfork bifurcation when leaving Sector IV by crossing Line 4 to Sector V ( $\mu_1 < 0$ ,  
 259  $\mu_2 < d\mu_1/b$ ). Equivalently, a torus bifurcation of  $P_2$  occurs in the infinite-dimensional system (2.1).  
 260 In Sector V, the equilibrium  $(0, r_2^P)$  becomes a source, while the equilibrium  $(r_1^P, 0)$  remains a  
 261 saddle and the trivial equilibrium remains a sink. Entering Sector VI ( $\mu_1 > 0$ ,  $\mu_2 < 0$ ) by crossing  
 262 Line 1, the equilibrium  $(r_1^P, 0)$  disappears via a pitchfork bifurcation, which corresponds to a  
 263 Hopf bifurcation of the trivial equilibrium of (2.1). Here, the equilibrium  $(0, r_2^P)$  remains a source  
 264 and the trivial equilibrium becomes a saddle. Finally, the equilibrium  $(r_2^P, 0)$  disappears via a  
 265 pitchfork bifurcation when returning to Sector I by crossing Line 2, i.e.,  $P_2$  vanishes as a result of  
 266 a Hopf bifurcation in the time-delay system (2.1).

267 A second example is presented in Fig. 2(b), where the intersection of the fourth ( $j_1 = 4$ ) and the  
 268 fifth ( $j_2 = 5$ ) stability lobes is shown, see also the square mark in Fig. 1(b). The parameters of the  
 269 double Hopf point, the corresponding root tendencies and the cubic coefficients are listed in the  
 270 second row of Tab. 1 and Tab. 2. In this example,  $a, b, c$  and  $d$  are positive but now  $A$  is negative,  
 271 thus Case Ib in [17] applies. In this case, the order of Lines 3 and 4 changes when going around  
 272 the sectors of the plane  $(\mu_1, \mu_2)$  anti-clockwise. Therefore, the quasi-periodic solution QP is born  
 273 from  $P_2$  (and not  $P_1$ ) when entering Sector IV along Line 4, and it collapses into  $P_1$  (and not  $P_2$ )  
 274 when leaving Sector IV along Line 3. Interchanging Lines 3 and 4 modifies the topology only in  
 275 Sector IV: now the equilibria  $(r_1^P, 0)$  and  $(0, r_2^P)$  are sources and the equilibrium  $(r_1^{QP}, r_2^{QP})$  is a  
 276 saddle. Consequently, the periodic solutions  $P_1$  and  $P_2$  behave as sources and the quasi-periodic  
 277 solution QP behaves as a saddle.

278 (b) Bifurcation Diagrams via Higher-Order Estimation

The amplitudes of the arising periodic and quasi-periodic orbits can be determined by calculating the non-trivial equilibria of (5.1). According to [17], they can be calculated as

$$\begin{aligned}
 P_1: \quad \bar{r}_1^P &= \sqrt{-\frac{\mu_1}{a}} & \Rightarrow \quad r_1^P(\hat{w}, \hat{\Omega}) &= \sqrt{-\frac{\gamma_{11}\hat{w} + \gamma_{12}\hat{\Omega}}{a_{11}}}, \\
 P_2: \quad \bar{r}_2^P &= \sqrt{-\frac{\mu_2}{d}} & \Rightarrow \quad r_2^P(\hat{w}, \hat{\Omega}) &= \sqrt{-\frac{\gamma_{21}\hat{w} + \gamma_{22}\hat{\Omega}}{a_{22}}}, \\
 QP: \quad \bar{r}_1^{QP} &= \sqrt{\frac{b\mu_2 - d\mu_1}{A}} & \Rightarrow \quad r_1^{QP}(\hat{w}, \hat{\Omega}) &= \sqrt{\frac{(a_{12}\gamma_{21} - a_{22}\gamma_{11})\hat{w} + (a_{12}\gamma_{22} - a_{22}\gamma_{12})\hat{\Omega}}{a_{11}a_{22} - a_{12}a_{21}}}, \\
 & \bar{r}_2^{QP} = \sqrt{\frac{c\mu_1 - a\mu_2}{A}} & \Rightarrow \quad r_2^{QP}(\hat{w}, \hat{\Omega}) &= \sqrt{\frac{(a_{21}\gamma_{11} - a_{11}\gamma_{21})\hat{w} + (a_{21}\gamma_{12} - a_{11}\gamma_{22})\hat{\Omega}}{a_{11}a_{22} - a_{12}a_{21}}}.
 \end{aligned}
 \tag{5.3}$$

279 Here we emphasise that the amplitudes depend on the two bifurcation parameters  $\hat{w}$  and  $\hat{\Omega}$ . Later  
 280 on we omit the argument  $(\hat{w}, \hat{\Omega})$  for simplicity.

281 In [45], it was show that a higher-order estimation of the amplitude of the periodic orbits  
 282 arising from Hopf bifurcation is possible when special global properties hold in the system. This  
 283 estimation can also be done for the quasi-periodic orbit arising from the double Hopf bifurcation.  
 284 The estimation is based on the approximation of the cubic coefficients  $a_{mn}$  ( $m, n = 1, 2$ ) by a linear  
 285 function of the bifurcation parameters  $\Omega, w$  instead of using the constant values defined by (4.29):

$$\hat{a}_{mn} = a_{mn} + a_{mn}^{\Omega}\hat{\Omega} + a_{mn}^w\hat{w}, \tag{5.4}$$

286  $m, n = 1, 2$ . Replacing  $a_{mn}$  with  $\hat{a}_{mn}$  in (5.3) yields a higher-order estimation of the amplitude of  
 287 the periodic and the quasi-periodic orbits as long as the additional coefficients  $a_{mn}^{\Omega}$  and  $a_{mn}^w$  are  
 288 chosen properly.

289 The additional coefficients can be calculated based on the following global properties of the  
 290 system. When the chip width is zero, that is,  $w = 0$ , the cutting force on the right-hand side  
 291 of the governing equation (2.1) vanishes and the system reduces to a damped free oscillator.  
 292 Hence the periodic and the quasi-periodic solutions must disappear at  $w = 0$ , which happens  
 293 such that their amplitudes tend to infinity. That is,  $\lim_{w \rightarrow 0} r_1^P = \infty$  and  $\lim_{w \rightarrow 0} r_2^P = \infty$  holds  
 294 for the periodic solutions, whereas  $\lim_{w \rightarrow 0} r_1^{QP} = \infty$  and  $\lim_{w \rightarrow 0} r_2^{QP} = \infty$  for the quasi-periodic  
 295 solution. Similarly, when  $\tau = 0$  or, equivalently,  $\Omega \rightarrow \infty$ , the right-hand side of (2.1) becomes  
 296 zero. Therefore, the periodic solutions satisfy  $\lim_{\Omega \rightarrow \infty} r_1^P = \infty$  and  $\lim_{\Omega \rightarrow \infty} r_2^P = \infty$ , whereas the  
 297 quasi-periodic solution satisfies  $\lim_{\Omega \rightarrow \infty} r_1^{QP} = \infty$  and  $\lim_{\Omega \rightarrow \infty} r_2^{QP} = \infty$ . It can be shown that  
 298 these properties are guaranteed with the coefficients

$$\hat{a}_{mn} = a_{mn} + \frac{a_{mn}}{w_{HH}}\hat{w}, \tag{5.5}$$

299  $m, n = 1, 2$ . Note that approximating the cubic coefficients by such linear functions of the  
 300 bifurcation parameters instead of using the constants in (4.29) does not change the formulae of  
 301 Lines 1-4 in (5.2).

The periodic and quasi-periodic solutions of (2.1) can be approximated as

$$\begin{aligned}
 \mathbf{y}_t(\theta) &\approx r_1(\hat{w}, \hat{\Omega}) (\cos(\omega_1 t)\mathbf{s}_{1,R}(\theta) - \sin(\omega_1 t)\mathbf{s}_{1,I}(\theta)) \\
 &\quad + r_2(\hat{w}, \hat{\Omega}) (\cos(\omega_2 t)\mathbf{s}_{2,R}(\theta) - \sin(\omega_2 t)\mathbf{s}_{2,I}(\theta)),
 \end{aligned}
 \tag{5.6}$$

$$x(t) = \mathbf{y}_{t1}(0) \approx r_1(\hat{w}, \hat{\Omega}) \cos(\omega_1 t) + r_2(\hat{w}, \hat{\Omega}) \cos(\omega_2 t), \tag{5.7}$$

302 where  $(r_1, r_2) = (r_1^P, 0)$  and  $(r_1, r_2) = (0, r_2^P)$  must be substituted for the periodic solutions  $P_1$   
 303 and  $P_2$ , respectively, whereas  $(r_1, r_2) = (r_1^{QP}, r_2^{QP})$  for the quasi-periodic solution QP with the  
 304 amplitudes given by (5.3) using  $\hat{a}_{mn}$  instead of  $a_{mn}$ . The bifurcation diagrams presenting the

305 amplitude of the periodic and the quasi-periodic solutions will be presented in Fig. 3 together  
 306 with the corresponding global stability charts.

### 307 (c) Global Dynamics and Region of Bistability

308 In the linearly stable region, where the equilibrium is a sink, the coexisting periodic and quasi-  
 309 periodic solutions are unstable. Due to these unstable orbits, the basin of attraction of the linearly  
 310 stable equilibrium is finite, hence the equilibrium is not stable in the global sense. To large enough  
 311 perturbations, the vibrations of the machine tool amplify in a self-excited manner.

312 When the vibration amplitude becomes large enough, the tool jumps out of the workpiece and  
 313 leaves the material during cutting. In such cases, the tool's motion is governed by non-smooth  
 314 dynamics: switching occurs between the dynamics of a cutting tool and the dynamics of a 'flying'  
 315 tool (a damped free oscillator). The switching surface is located where the chip thickness is zero  
 316 and loss of contact takes place. If the tool loses contact with the workpiece and undergoes a free  
 317 flight, then (2.1) becomes no longer valid, since the cutting force on the right-hand side vanishes.  
 318 It was shown in [14] for the case of the single Hopf bifurcation that once the unstable periodic  
 319 motion involves loss of contact and grazes the switching surface, the periodic orbit undergoes  
 320 a kind of non-smooth fold of limit cycles bifurcation called Big Bang Bifurcation (B<sup>3</sup>). This  
 321 bifurcation is illustrated in Fig. 1(c) for  $j = 2$ ,  $\omega = 1.37$  ( $\Omega = 0.901$ ) as shown by the dashed line  
 322 in Fig. 1(b). Via the non-smooth fold, the unstable periodic orbit vanishes by merging with a  
 323 large-amplitude attractive solution. This solution describes machine tool chatter with intermittent  
 324 loss of contact, it may be chaotic and it coexists with the unstable periodic orbit and the linearly  
 325 stable equilibrium. The region of coexistence is also called unsafe zone or region of bistability.  
 326 Determining the boundary of the bistable region is important, since the cutting process unsafe in  
 327 this region: it is stable only linearly but not in the global sense.

328 We can expect similar behaviour in the vicinity of the double Hopf point. Periodic and  
 329 quasi-periodic solutions exist only up to the point where the tool first loses contact with the  
 330 workpiece during its large-amplitude motion. Thus, a Big Bang Bifurcation happens where the  
 331 dimensionless chip thickness  $h(t)$  first drops to zero, that is, when

$$h(t) = 1 + x(t - \tau) - x(t) = 0 \quad (5.8)$$

occurs for any  $t$ . Equation (5.8) defines the loci of the Big Bang Bifurcation and gives the boundary  
 of the bistable region for the periodic and the quasi-periodic solutions. Substituting (5.7) into (5.8),  
 combining the trigonometric terms and approximating  $\tau \approx \tau_{HH}$ , we get

$$r_1(\hat{w}, \hat{\Omega}) \sqrt{(1 - \cos(\omega_1 \tau_{HH}))^2 + \sin^2(\omega_1 \tau_{HH}) \cos(\omega_1 t + \phi_1)} \\ + r_2(\hat{w}, \hat{\Omega}) \sqrt{(1 - \cos(\omega_2 \tau_{HH}))^2 + \sin^2(\omega_2 \tau_{HH}) \cos(\omega_2 t + \phi_2)} = 1, \quad (5.9)$$

332 where  $\phi_1$  and  $\phi_2$  are certain phase shifts. If there exists any  $t$  for which (5.9) holds, then loss  
 333 of contact takes place and the periodic or the quasi-periodic solutions disappear. The smallest  
 334 amplitude for which loss of contact might occur is obtained by substituting  $\cos(\omega_1 t + \phi_1) = 1$   
 335 and  $\cos(\omega_2 t + \phi_2) = 1$ . This motivates the introduction of the scaled amplitude

$$r := r_1(\hat{w}, \hat{\Omega}) \sqrt{2(1 - \cos(\omega_1 \tau_{HH}))} + r_2(\hat{w}, \hat{\Omega}) \sqrt{2(1 - \cos(\omega_2 \tau_{HH}))} \quad (5.10)$$

336 and  $r = 1$  indicates loss of contact. If  $r > 1$ , then the periodic and the quasi-periodic solutions  
 337 disappear via the Big Bang Bifurcation. Note that the quasi-periodic solution is located on an  
 338 invariant torus. Taking  $\cos(\omega_1 t + \phi_1) = 1$  and  $\cos(\omega_2 t + \phi_2) = 1$  implies that the solution is  
 339 assumed to be dense where the torus touches the switching surface (5.8).

340 Taking  $r = 1$ , substituting the higher-order estimation of the amplitude of the periodic  
 341 solutions given by (5.3) with  $\hat{a}_{mn}$  instead of  $a_{mn}$ , we can obtain the boundary where the periodic

342 solutions disappear via a Big Bang Bifurcation in the form

$$\hat{w}_{P_k}^{B^3}(\hat{\Omega}) = -\frac{\gamma_{k2}\hat{\Omega} + \frac{a_{kk}}{2(1 - \cos(\omega_k\tau_{HH}))}}{\gamma_{k1} + \frac{a_{kk}}{2w_{HH}(1 - \cos(\omega_k\tau_{HH}))}}. \quad (5.11)$$

343 The boundary  $\hat{w}_{QP}^{B^3}(\hat{\Omega})$  where the quasi-periodic solution vanishes can be determined the same  
 344 way by symbolic algebra (the resulting formula is too long to be presented here). If any of the  
 345 unstable periodic or quasi-periodic solutions exists, a large-amplitude attractive solution coexists  
 346 with the stable equilibrium. Therefore, the boundary of the bistable region is determined by those  
 347 Big Bang Bifurcation curves, which are the farthest from the linear stability boundary.

348 The results are summarised in Fig. 3 where the double Hopf points (DH) at the intersections  
 349 of the first and the second, the second and the third, and the fourth and the fifth lobes are  
 350 considered in rows (a), (b) and (c), respectively. In each panel, the analytical results are indicated  
 351 by solid lines. The left panels show the stability charts of the system. The right panels show the  
 352 corresponding bifurcation diagrams with the amplitude  $r$  of the periodic orbits  $P_1$ ,  $P_2$  and the  
 353 quasi-periodic orbit QP as a function of the bifurcation parameter  $w$ . Parameter  $\Omega$  is fixed to  
 354  $\Omega = 1.0095$ ,  $\Omega = 0.505$  and  $\Omega = 0.2527$  in rows (a), (b) and (c), respectively, which correspond  
 355 to the dotted vertical lines in the left panels. In the left panels, solid thick blue and cyan lines  
 356 show the intersecting stability lobes given by (3.3), whereas their tangents (Lines 1 and 2) are  
 357 indicated by thin blue and cyan lines. Note that in the region depicted, Line 2 overlaps with the  
 358 solid thick cyan stability lobe. In the right panels, the periodic orbits  $P_1$  and  $P_2$  initiate from the  
 359 (approximate) Hopf bifurcation points  $H(P_1)$  and  $H(P_2)$ , which correspond to the intersections  
 360 of the dotted line with Lines 1 and 2 in the left panels of Fig. 3, respectively. The periodic orbits  
 361 undergo a torus bifurcation along the red and purple lines (Lines 3 and 4) in the left panels. In  
 362 the right panel of Fig. 3(a), the quasi-periodic solution QP is born from the periodic solution  $P_1$   
 363 through a torus bifurcation at  $T(P_1)$ , which corresponds to the intersection of the dotted line and  
 364 Line 3 in the left panel. In Figs. 3(b) and 3(c), the quasi-periodic orbit QP arises from the other  
 365 periodic solution  $P_2$  through a torus bifurcation at  $T(P_2)$ , see also the intersection of the dotted  
 366 line and Line 4 in the left panels.

367 The bifurcation diagrams in the right panels of Fig. 3 are valid only up to points  $B^3(P_1)$ ,  
 368  $B^3(P_2)$  and  $B^3(QP)$  at  $r = 1$ , where (2.1) becomes invalid due to loss of contact between the  
 369 tool and the workpiece. The branches are invalid for  $r > 1$ , the periodic and the quasi-periodic  
 370 solutions vanish there and large-amplitude stable solutions are born via a non-smooth fold. In the  
 371 left panels, solid green and orange lines show the loci of Big Bang Bifurcation given by (5.11) for  
 372 the periodic orbits  $P_1$  and  $P_2$ , respectively. The Big Bang Bifurcation curve for the quasi-periodic  
 373 solution is shown by a black line. Dark gray shading shows the regions where the periodic orbits  
 374 indeed exist, that is, without losing contact with the workpiece. Similarly, darker gray shading  
 375 indicates the region where the quasi-periodic solution exists. Light gray shading indicates the  
 376 region where no periodic or quasi-periodic orbits exist due to loss of contact. Only the stable  
 377 equilibrium exists here, hence the system is globally stable. In the regions with dark gray and  
 378 darker gray shading, the system is bistable. Based on the figure, the quasi-periodic orbit occurs  
 379 in a narrow range of parameters and does not affect the boundary of the globally stable region.  
 380 Consequently, even close to the intersection of the stability lobes, the globally stable region can be  
 381 determined by the formulas obtained from the analysis of the single Hopf bifurcation [11].

382 We calculated the amplitude of solutions by numerical continuation as well, see the dashed  
 383 lines in Fig. 3. We used DDE-BIFTOOL [40] for the computation of the periodic orbits, and  
 384 used the algorithm in [15,41] to compute the quasi-periodic orbit. The loci of torus and Big  
 385 Bang Bifurcations have also been continued in two parameters, see the dashed lines in the left  
 386 panels. Note that the analytical results are only approximations and the numerical results can  
 387 be considered as exact ones. We can see that the analytical results give only the tangents of  
 388 the numerical torus bifurcation branches. The agreement between the analytical and numerical  
 389 results is better in the right panels of Figs. 3(b) and 3(c) than in Fig. 3(a). At the intersection of the

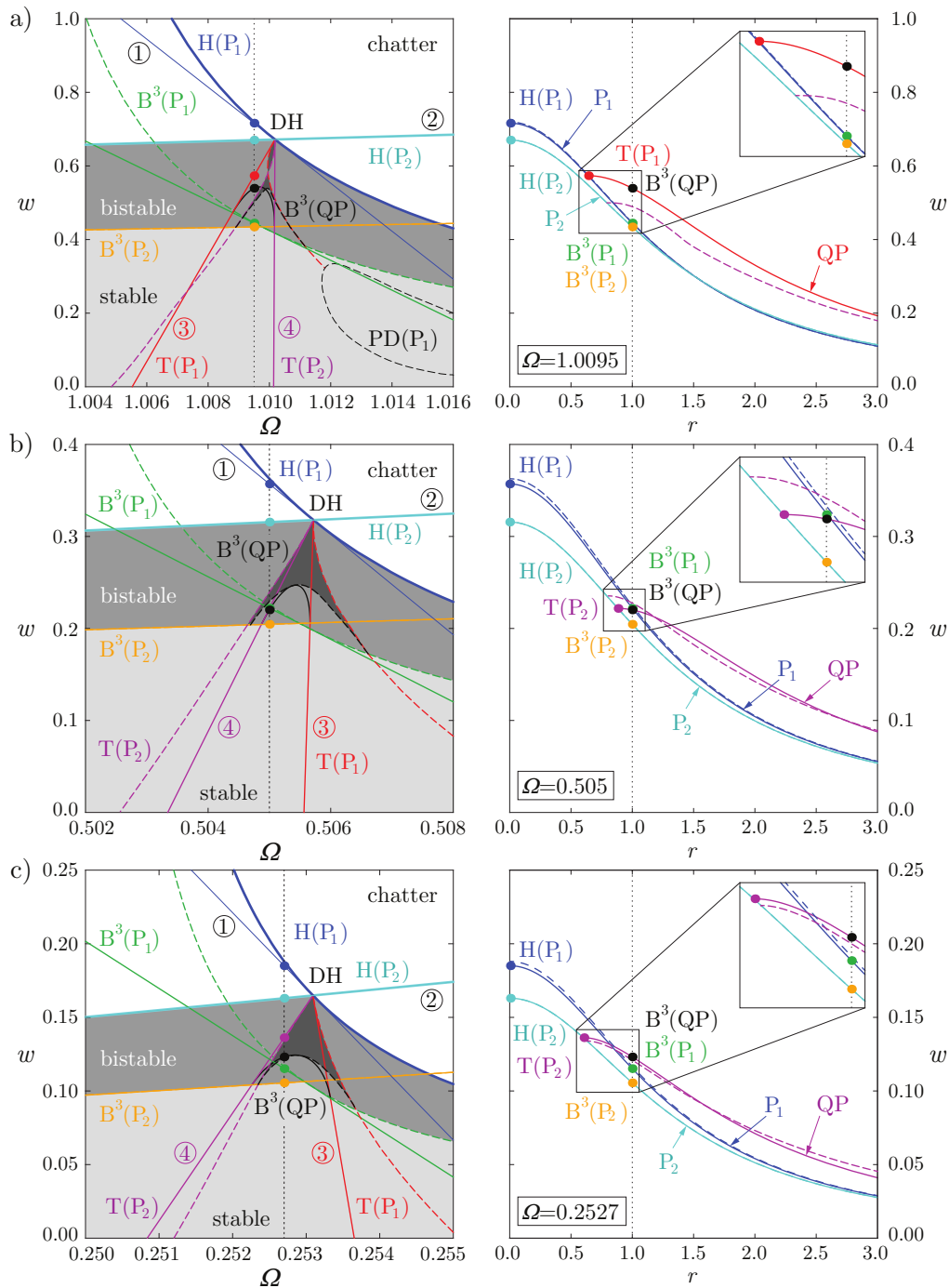


**Figure 3.** Stability charts (left) and bifurcation diagrams (right) close to the double Hopf point (DH) at the intersection of the first and the second lobe (a); the second and the third lobe (b); the fourth and the fifth lobe (c). Analytical results are indicated by solid lines and dashed lines show the numerical results. Blue and cyan lines show the loci of Hopf bifurcation (H) where periodic solutions ( $P_1$  and  $P_2$ ) are born. Red and purple lines represent the loci of torus bifurcation (T) where a quasi-periodic orbit (QP) emerges from one of the periodic orbits. Green, orange and black lines indicate the loci of Big Bang Bifurcation ( $B^3$ ) where the tool loses contact with the workpiece during periodic or quasi-periodic oscillations. Thin black line indicates period doubling bifurcation (PD). The globally stable region is indicated by light gray shading, whereas dark gray and darker gray shadings show the bistable regions where unstable periodic and quasi-periodic solutions coexist with the linearly stable equilibrium and the large-amplitude stable motion (chatter) that involves loss of contact.



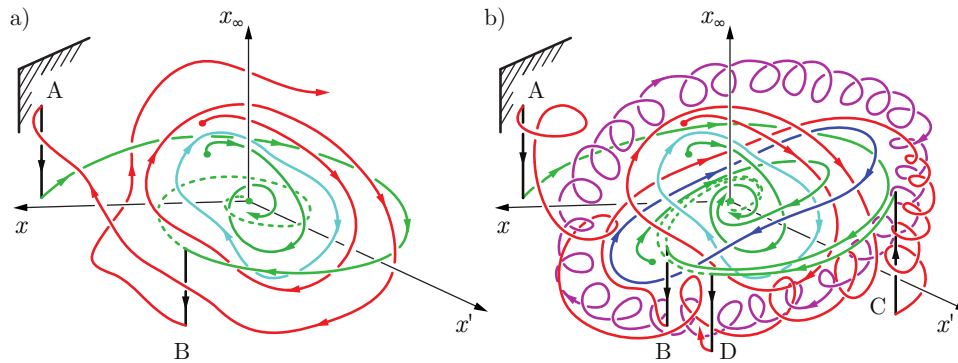


**Figure 4.** Trajectories of the cutting process in the neighbourhood of a single periodic orbit (a); trajectories where two periodic orbits coexist with a quasi-periodic one (b).

390 first and the second stability lobes in Fig. 3(a), the analytical results for the torus bifurcation curves  
 391 are valid only in the close vicinity of the double Hopf point, then the numerical branches deviate.  
 392 Therefore, the analytical bifurcation diagram in the right panel is not accurate even qualitatively:  
 393 the quasi-periodic solution is born from the other periodic solution as in the numerical case. The  
 394 numerical counterparts of the Big Bang Bifurcation branches  $B^3(P_1)$  and  $B^3(P_2)$  are also shown  
 395 by dashed green and orange lines in the left panels of Fig. 3. Again, the analytical results give  
 396 only the tangents of the numerical branches. Note that the solid and dashed orange lines overlap.  
 397 The dashed green and orange lines can also be obtained by analytical formulae using the results of  
 398 [11,45] on the single Hopf bifurcation, which considers the entire stability lobes not only their  
 399 intersection. In addition, numerical continuation showed that even a period doubling bifurcation  
 400 of the periodic solution  $P_1$  can occur, see the dashed thin black line  $PD(P_1)$  in the left panel of  
 401 Fig. 3(a). However, this branch lies beyond the Big Bang Bifurcation  $B^3(P_1)$ , hence the period  
 402 doubling does not show up when considering loss of contact between the tool and the workpiece.

403 Finally, Fig. 4 shows a qualitative picture about the trajectories of the infinite-dimensional  
 404 non-smooth system including loss of contact between the tool and the workpiece. The infinite-  
 405 dimensional phase space is illustrated by three axes:  $x$  and  $x'$ , which are the general coordinates of  
 406 the corresponding delay-free system, and  $x_\infty$ , which is introduced only for illustration purposes  
 407 to represent the other infinitely many dimensions as a cumulative effect of the past. Panel  
 408 (a) shows the case where only a single periodic orbit (cyan line) exists in the vicinity of the  
 409 equilibrium. Here, the trajectories which lie within the basin of attraction of the equilibrium tend  
 410 towards the equilibrium, see the solely green trajectory. However, the basin of attraction is finite  
 411 and trajectories lying outside spiral outwards, see the red line. In this case, the vibrations amplify  
 412 until the trajectory hits the switching surface (5.8) indicated by hatches at point A. Here, the  
 413 tool jumps out of the workpiece. When the tool is out of contact, the infinite-dimensional system  
 414 reduces to a two-dimensional one as shown by the black line. Temporarily, the system behaves  
 415 as a damped free oscillator, which is illustrated by the trajectories spiralling towards the origin  
 416 in the plane  $(x, x')$  (see the green line). The amplitude of the vibrations decreases until the tool gets  
 417 back into the workpiece at point B. The system becomes infinite-dimensional again (black line)  
 418 and the trajectory diverges from the origin again (red line).

419 Figure 4(b) shows the case where two periodic solutions (blue and cyan lines) and a quasi-  
 420 periodic solution (purple line) coexist, cf. Sector IV in Fig. 2. The green trajectories lie within the  
 421 basin of attraction of the equilibrium, hence they spiral towards the origin. The red trajectory lies  
 422 outside and diverges from the origin. Note that this red trajectory is only a possible example, and  
 423 it can be considered as the representation of the red lines in Sector IV of Fig. 2(b). The solution  
 424 initiates in the vicinity of one periodic solution, cf. the upper red curve in Fig. 2(b). The trajectory  
 425 spirals outwards, wraps around the quasi-periodic solution, and runs until it hits the switching

426 surface (5.8) at point A, see the hatches in Fig. 4(b) and the dashed line in Fig. 2(b). Here, the  
 427 tool gets out of the workpiece (black line), the system becomes two-dimensional and restricted to  
 428 plane  $(x, x')$ , where the trajectory spirals towards the origin (green line). Then, the tool enters the  
 429 workpiece at point B (black line) and the solution continues in the vicinity of the other periodic  
 430 orbit (red line), cf. the lower red curve in Fig. 2(b). The vibrations start amplifying again until the  
 431 contact between the tool and the workpiece is lost at point C (black line). A damped motion  
 432 (green line) follows in the plane  $(x, x')$  until point D is reached. The tool gets back into the  
 433 workpiece again (black line) and, once more, the infinite-dimensional dynamics prevails. The  
 434 whole trajectory may even describe chaotic motion. The chaos can be transient, since it can occur  
 435 that, after a while, the trajectory penetrates the basin of attraction of the equilibrium when the tool  
 436 gets back into the workpiece. Then, at last, the system becomes globally stable and the trajectory  
 437 approaches the origin.

## 438 6. Conclusions

439 In this paper, we investigated the dynamics of machine tool vibrations in the vicinity of a double  
 440 Hopf bifurcation point. Via center manifold reduction, we derived the normal form coefficients of  
 441 the four-dimensional center subsystem, which determines the long-term dynamics in the vicinity  
 442 of the double Hopf point. Based on the normal form coefficients, we identified the possible  
 443 topologies in the phase space of the four-dimensional center subsystem. We found the previously  
 444 unexplored Case Ia of [17] and also the Case Ib that was predicted in [27], and showed that  
 445 unstable periodic and quasi-periodic solutions coexist with the linearly stable equilibrium in  
 446 certain parameter regions. Taking loss of contact between the tool and the workpiece into account,  
 447 we derived the approximate boundaries of the globally stable region in closed form. We verified  
 448 the results by numerical continuation using DDE-BIFTOOL [40] and the algorithm of [15,41],  
 449 which even revealed the existence of period doubling bifurcation of periodic orbits. Finally, we  
 450 assessed qualitatively the non-smooth global dynamics in the infinite-dimensional phase space  
 451 and pointed out the possibility of transient chaotic motions.

452 **Ethics.** This work did not involve any research on humans or animals.

453 **Data Accessibility.** This work does not have any experimental data.

454 **Authors' Contributions.** Tamas G. Molnar was responsible for the analytical bifurcation analysis, Zoltan  
 455 Dombóvári carried out the numerical continuation. Gabor Stepan and Tamas Insperger supervised the project.  
 456 All authors contributed to writing the paper and gave final approval for publication.

457 **Competing Interests.** We declare we have no competing interests.

458 **Funding.** This work has been supported by the ÚNKP-16-3-I. New National Excellence Program of the  
 459 Ministry of Human Capacities. This work has received funding from the János Bolyai Research Scholarship  
 460 of MTA (BO/00589/13/6). The research leading to these results has received funding from the European  
 461 Research Council under the European Union's Seventh Framework Programme (FP/2007-2013) / ERC  
 462 Advanced Grant Agreement n. 340889.

## 463 References

- 464 1. S. A. Tobias, W. Fishwick, Theory of regenerative machine tool chatter, *The Engineer* (1958)  
 465 199–203, 238–239.
- 466 2. J. Tlustý, M. Polacek, The stability of the machine tool against self-excited vibration in  
 467 machining, in: *ASME Production Engineering Research Conference*, Pittsburgh, 1963, pp.  
 468 454–465.
- 469 3. J. Hale, *Theory of Functional Differential Equations*, Springer, New York, 1977.
- 470 4. G. Stépán, Z. Dombóvári, J. Muñoa, Identification of cutting force characteristics based on  
 471 chatter experiments, *CIRP Annals - Manufacturing Technology* 60 (1) (2011) 113–116.
- 472 5. H. M. Shi, S. A. Tobias, Theory of finite amplitude machine tool instability, *International*  
 473 *Journal of Machine Tool Design and Research* 24 (1) (1984) 45–69.

- 474 6. W. J. Endres, M. Loo, Modeling cutting process nonlinearity for stability analysis - application  
475 to tooling selection for valve-seat machining, in: 5th CIRP International Workshop on  
476 Modeling of Machining, West Lafayette, IN, USA, 2002, pp. 71–82.
- 477 7. N. K. Chandiramani, T. Pothala, Dynamics of 2-dof regenerative chatter during turning,  
478 Journal of Sound and Vibration 290 (1–2) (2006) 448–464.
- 479 8. K. Ahmadi, F. Ismail, Experimental investigation of process damping nonlinearity in  
480 machining chatter, International Journal of Machine Tools and Manufacture 50 (11) (2010)  
481 1006–1014.
- 482 9. G. Stépán, T. Kalmár-Nagy, Nonlinear regenerative machine tool vibrations, in: Proceedings  
483 of DETC'97, ASME Design and Technical Conferences, Sacramento, CA, USA, 1997, pp. 1–11.
- 484 10. T. Kalmár-Nagy, G. Stépán, F. C. Moon, Subcritical Hopf bifurcation in the delay equation  
485 model for machine tool vibrations, Nonlinear Dynamics 26 (2001) 121–142.
- 486 11. Z. Dombóvári, R. E. Wilson, G. Stépán, Estimates of the bistable region in metal cutting,  
487 Proceedings of the Royal Society A - Mathematical, Physical and Engineering Sciences 464  
488 (2008) 3255–3271.
- 489 12. A. H. Nayfeh, Order reduction of retarded nonlinear systems – the method of multiple scales  
490 versus center-manifold reduction, Nonlinear Dynamics 51 (4) (2008) 483–500.
- 491 13. K. Nandakumar, P. Wahi, A. Chatterjee, Infinite dimensional slow modulations in a well  
492 known delayed model for cutting tool vibrations, Nonlinear Dynamics 62 (4) (2010) 705–716.
- 493 14. Z. Dombóvári, D. A. Barton, R. E. Wilson, G. Stépán, On the global dynamics of chatter in  
494 the orthogonal cutting model, International Journal of Non-Linear Mechanics 46 (1) (2011)  
495 330–338.
- 496 15. Z. Dombóvári, G. Stépán, On the bistable zone of milling processes, Philosophical  
497 Transactions of the Royal Society A: Mathematical, Physical and Engineering Sciences 373  
498 (2015) 20140409.
- 499 16. B. D. Hassard, N. D. Kazarinoff, Y.-H. Wan, Theory and Applications of Hopf Bifurcation,  
500 London Mathematical Society Lecture Note Series 41, Cambridge, 1981.
- 501 17. J. Guckenheimer, P. Holmes, Nonlinear Oscillations, Dynamical Systems, and Bifurcations of  
502 Vector Fields, Springer, New York, 1983.
- 503 18. G. Stépán, Retarded dynamical systems, Longman, Harlow, 1989.
- 504 19. Y. A. Kuznetsov, Elements of Applied Bifurcation Theory, Springer, New York, 1998.
- 505 20. S. A. Campbell, Calculating centre manifolds for delay differential equations using maple, in:  
506 B. Balachandran, T. Kalmár-Nagy, D. E. Gilsinn (Eds.), Delay Differential Equations, Springer,  
507 New York, 2009, pp. 221–244.
- 508 21. A. H. Nayfeh, D. T. Mook, Nonlinear Oscillations, Wiley, New York, 1979.
- 509 22. J. Hale, Averaging methods for differential equations with retarded arguments and a small  
510 parameter, Journal of Differential Equations 2 (1) (1966) 57–73.
- 511 23. J. Hale, S. M. V. Lunel, Averaging in infinite dimensions, Journal of Integral Equations and  
512 Applications 2 (4) (1990) 463–494.
- 513 24. B. Lehman, S. P. Weibel, Fundamental theorems of averaging for functional differential  
514 equations, Journal of Differential Equations 152 (1) (1999) 160–190.
- 515 25. J. A. Sanders, F. Verhulst, J. Murdock, Averaging Methods in Nonlinear Dynamical Systems,  
516 Springer, New York, 2007.
- 517 26. T. Sari, Averaging for ordinary differential equations and functional differential equations, in:  
518 I. van den Berg, V. Neves (Eds.), The Strength of Nonstandard Analysis, Springer, Wien, 2007,  
519 pp. 286–305.
- 520 27. G. Stépán, Modelling nonlinear regenerative effects in metal cutting, Philosophical  
521 Transactions of the Royal Society A: Mathematical, Physical and Engineering Sciences  
522 359 (1781) (2001) 739–757.
- 523 28. S. A. Campbell, J. Bélair, T. Ohira, J. Milton, Limit cycles, tori, and complex dynamics in a  
524 second-order differential equation with delayed negative feedback, Journal of Dynamics and  
525 Differential Equations 7 (1) (1995) 213–236.
- 526 29. G. Stépán, G. Haller, Quasiperiodic oscillations in robot dynamics, Nonlinear Dynamics 8 (4)  
527 (1995) 513–528.
- 528 30. S. A. Campbell, V. G. LeBlanc, Resonant Hopf-Hopf interactions in delay differential  
529 equations, Journal of Dynamics and Differential Equations 10 (2) (1998) 327–346.
- 530 31. J. Xu, K.-W. Chung, C.-L. Chan, An efficient method for studying weak resonant double  
531 Hopf bifurcation in nonlinear systems with delayed feedbacks, SIAM Journal on Applied  
532 Dynamical Systems 6 (1) (2007) 29–60.

- 533 32. S. Guo, Y. Chen, J. Wu, Two-parameter bifurcations in a network of two neurons with multiple  
534 delays, *Journal of Differential Equations* 244 (2) (2008) 444–486.
- 535 33. S. Ma, Q. Lu, Z. Feng, Double Hopf bifurcation for Van der Pol-Duffing oscillator with  
536 parametric delay feedback control, *Journal of Mathematical Analysis and Applications* 338 (2)  
537 (2008) 993–1007.
- 538 34. W. Wang, J. Xu, Multiple scales analysis for double Hopf bifurcation with 1:3 resonance,  
539 *Nonlinear Dynamics* 66 (1) (2011) 39–51.
- 540 35. C. Bazăs, A. R. Champneys, C. J. Hó, Bifurcation analysis of a simplified model of a pressure  
541 relief valve attached to a pipe, *SIAM Journal on Applied Dynamical Systems* 13 (2) (2014)  
542 704–721.
- 543 36. R. Qesmi, M. A. Babram, Double Hopf bifurcation in delay differential equations, *Arab*  
544 *Journal of Mathematical Sciences* 20 (2) (2014) 280–301.
- 545 37. Z. Shen, C. Zhang, Double Hopf bifurcation of coupled dissipative Stuart-Landau oscillators  
546 with delay, *Applied Mathematics and Computation* 227 (2014) 553–566.
- 547 38. Y. Ding, J. Cao, W. Jiang, Double Hopf bifurcation in active control system with delayed  
548 feedback: application to glue dosing processes for particleboard, *Nonlinear Dynamics* 83 (3)  
549 (2016) 1567–1576.
- 550 39. P. Wahi, A. Chatterjee, Regenerative tool chatter near a codimension 2 Hopf point using  
551 multiple scales, *Nonlinear Dynamics* 40 (4) (2005) 323–338.
- 552 40. K. Engelborghs, T. Luzyanina, D. Roose, Numerical bifurcation analysis of delay differential  
553 equations using DDE-BIFTOOL, *ACM Transactions on Mathematical Software* 28 (1) (2002)  
554 1–21.
- 555 41. D. Roose, R. Szalai, Continuation and bifurcation analysis of delay differential equations, in:  
556 B. Krauskopf, H. M. Osinga, J. Galán-Vioque (Eds.), *Numerical continuation methods for*  
557 *dynamical systems: Path following and boundary value problems*, Springer Netherlands,  
558 2007, pp. 359–399.
- 559 42. R. Szalai, Knut: A continuation and bifurcation software for delay-differential equations,  
560 <http://rs1909.github.io/knut/> (2005–2013).
- 561 43. E. Knobloch, Normal form coefficients for the nonresonant double Hopf bifurcation, *Physics*  
562 *Letters A* 116 (8) (1986) 365–369.
- 563 44. W. Wang, J. Xu, X. Sun, Strong and weak resonances in delayed differential systems,  
564 *International Journal of Bifurcation and Chaos* 23 (7) (2013) 1350119.
- 565 45. T. G. Molnár, T. Insperger, G. Stépán, Analytical estimations of limit cycle amplitude for  
566 delay-differential equations, *Electronic Journal of Qualitative Theory of Differential Equations*  
567 2016 (77) (2016) 1–10.